HHS Public Access

Author manuscript

Nat Cell Biol. Author manuscript; available in PMC 2021 July 06.

Published in final edited form as:

Nat Cell Biol. 2019 December ; 21(12): 1578–1589. doi:10.1038/s41556-019-0433-z.

Phase separation of YAP reorganizes genome topology for long-term YAP target gene expression

Danfeng Cai[1,2], **Daniel Feliciano**[2,3], **Peng Dong**[2], **Eduardo Flores**[4], **Martin Gruebele**[5], **Natalie Porat-Shliom**[3], **Shahar Sukenik**[4,5], **Zhe Liu**[2], **Jennifer Lippincott-Schwartz**[2,*]

[1]Eunice Kennedy Shriver National Institute for Child Health and Human Development, National Institute of Health, Bethesda, Maryland 20892

[2]Janelia Research Campus, Howard Hughes Medical Institute, Ashburn, Virginia 20147

[3]Thoracic and Malignancies Branch, National Cancer Institute, National Institute of Health, Bethesda, Maryland 20892

[4]Department of Chemistry and Chemical Biology, University of California, Merced, California 95343

[5]Department of Chemistry, University of Illinois at Urbana–Champaign, Urbana, Illinois 61801

Abstract

Yes-associated Protein (YAP) is a transcriptional co-activator that regulates cell proliferation and survival by binding to a select set of enhancers for target gene activation. How YAP coordinates these transcriptional responses is unknown. Here, we demonstrate that YAP forms liquid-like condensates in the nucleus. Formed within seconds of hyperosmotic stress, YAP condensates compartmentalized YAP's transcription factor TEAD1 and other YAP-related co-activators, including TAZ, and subsequently induced transcription of YAP-specific proliferation genes. Super-resolution imaging using Assay for Transposase Accessible Chromatin with photoactivated localization microscopy (ATAC-PALM) revealed that YAP nuclear condensates were areas enriched in accessible chromatin domains organized as super-enhancers. Initially devoid of RNA Polymerase II (RNAPII), the accessible chromatin domains later acquired RNAPII, transcribing RNA. Removal of YAP's intrinsically-disordered transcription activation domain (TAD) prevented YAP condensate formation and diminished downstream YAP signaling. Thus, dynamic changes in genome organization and gene activation during YAP reprogramming is mediated by liquid-liquid phase separation.

Nuclear localization of the transcriptional co-activator YAP and activation of the TEA domain family (TEAD) transcription factors promote cell proliferation, differentiation and

*Correspondence to: lippincottschwartzj@janelia.hhmi.org.

Author Contributions

D.C. and J.L.-S. conceived and designed the study. D.C., D.F., P.D., E.F., and S.S. performed experiments. D.C. and J.L.-S. wrote the manuscript with constructive inputs from all authors. M.G., N.P.-S., S.S., Z.L. provided supervision.

Competing Interest

There is NO Competing Interest.

stem cell fate[1-3], with deficiencies in YAP regulation leading to developmental defects and cancer progression[1]. YAP's nuclear localization is regulated by the Hippo pathway, an evolutionarily conserved signaling pathway that responds to mechano-chemically induced changes in tissue architecture and osmolarity[4-6]. Despite YAP's importance, little is known regarding the precise mechanisms that lead to alteration of gene expression patterns when YAP is redistributed into the nucleus.

Phase separation of proteins and nucleic acids into liquid-like or gel-like condensates (also called 'droplets') in cells arises through a process involving weak multi-valent interactions among these molecules[7-9]. In the nucleus, such phase separation has recently been shown to contribute to heterochromatin formation[10,11], transcriptional upregulation[12-14], and clustering of nuclear enhancer elements and bound transcription-related factors into sites called super-enhancers (SEs)[15], which transcribe discrete sets of genes important for cell identity or cancer malignancy[15,16].

YAP has been shown to interact with various transcription elongation factors and can act at SE regions in the genome[17,18]. Given this and the above-mentioned suggestion of liquid-liquid phase separation involvement in SE formation, we investigated whether YAP forms phase condensates to activate its gene expression program. As prior work has shown that hyperosmotic stress activates YAP downstream signaling, we examined YAP localization upon hyperosmotic stress. We found that YAP formed nuclear and cytoplasmic phase condensates immediately upon hyperosmotic stress. The condensates contained different sets of proteins that contributed both to YAP's ability to redistribute into the nucleus and to its role in transcriptional control. In the nucleus, YAP droplets were shown to reorganize the genome for driving long-term, YAP target gene expression.

RESULTS

YAP has an intrinsic ability to phase separate into condensates

Analysis of YAP's amino acid sequence using algorithms predictive of disordered regions in proteins revealed YAP has an extended C-terminal low complexity region (LCR) encompassing a trans-activating domain (TAD) (Fig. 1a), known to mediate phase separation in other transcription cofactors[13]. To assess whether YAP can form liquid condensates *in vitro*, the non-ionic crowder PEG was added to purified EGFP-YAP from *E. coli*. This produced a turbid EGFP-YAP solution, in contrast to that found for purified EGFP (Fig. 1b, c). Confocal imaging of EGFP-YAP revealed the formation of micron-sized spheres under crowding conditions (Fig. 1d). The spheres displayed liquid-like condensate characteristics[19], including droplet coalescence (Fig. 1e), wetting the coverslip (Movie S1) and the ability to disperse upon resuspension in buffer with no crowder (Fig. 1d, washed). The reversibility of the EGFP-YAP droplets showed they were not aggregated particles incapable of rapidly disassembling. Other conditions known to affect phase separation of proteins (i.e., salts, inert proteins, and nucleic acids)[19,20] did not trigger YAP droplet formation (Extended Data Fig. 1a). The intrinsically-disordered TAD domain of YAP was required for YAP phase separation since YAP lacking this domain (i.e., EGFP-YAPΔTAD) failed to undergo phase separation under crowding concentrations similar to that seen for EGFP-YAP (Extended Data Fig. 1b).

YAP undergoes phase separation into cytoplasmic and nuclear condensates in hyperosmotically stressed cells

YAP is known to redistribute into the nucleus to drive transcription of proliferation-specific genes under conditions such as hyperosmotic stress[6]. We found that within 3 h of adding the hyperosmotic reagent *D*-sorbitol (0.2M) to HEK293T cells, transcription of YAP target genes Ctgf and Cyr61 increased by 6-fold and 3-fold, respectively (Fig. 2a). Similar results were seen in response to PEG300 addition (Fig. 2b).

Examining how hyperosmotic stress impacts YAP's subcellular distribution, we observed that EGFP-YAP shifted from being uniformly dispersed in the cytoplasm to being concentrated in discrete puncta in the cytoplasm and nucleus (Fig. 2c, top panel). The puncta formed within 20s of sorbitol treatment, and in zoomed-in images appeared spherical (Fig. 2d). EGFP expressed in these cells showed no change in subcellular distribution upon hyperosmotic stress (Fig. 2c, lower panel). The EGFP-YAP puncta persisted for 1 h and then decreased in number until a few nuclear condensates were left after 3 h in sorbitol (Fig. 2c, upper panel; Fig. 2e). Washing in isotonic medium when the puncta were still present caused the puncta to completely disappear within 5 min (Figs. 2f, g).

The EGFP-YAP puncta in hyperosmotically stressed cells exhibited key features of phase-separated condensates[7,21], including high sphericity (Extended Data Fig. 2a), fusion behavior (Fig. 2h, Movie S2-S4), and rapid fluorescence recovery upon photobleaching ($t_{1/2}$ = 0.9 ± 0.4 sec, Figs. 2i, j). Formation of these puncta was YAP isoform-independent (Extended Data Fig. 2b), not limited to the specific osmotic agent used (Extended Data Fig. 2c), and occurred in many cell types (Extended Data Fig. 2d), all of which underwent volume reduction (Extended Data Fig. 2e) and showed increased macromolecular crowding (Extended Data Figs. 2f, g) in response to the hyperosmotic stress.

Endogenous YAP in cells forms condensates

Using a YAP-specific antibody to label endogenous YAP in HEK293 cells, we found that within 10 min of sorbitol treatment, small puncta became visible in the nucleus (Fig. 3a). Like EGFP-YAP, the antibody-labeled condensates dissipated after 3 h of sorbitol treatment. Knocking down YAP by RNAi reduced YAP protein expression measured by immunoblotting and immunofluorescence (Extended Data Figs. 3a, b) and eliminated the YAP foci observed in response to sorbitol treatment (Fig. 3b).

We also generated a CRISPR knock-in U-2 OS cell line, fusing HaloTag to the C-terminus of the YAP genomic loci to generate cells with endogenous YAP replaced with YAP-HaloTag (Extended Data Fig. 3c). YAP-HaloTag nuclear puncta appeared within 10 min of hyperosmotic stress induced by either 0.2 M sorbitol (Figs. 3c, d) or 10% PEG300 (Extended Data Figs. 3d, e). The puncta recovered rapidly after photobleaching (Fig. 3e) and could be decorated with anti-YAP antibodies (Fig. 3f). Knocking down YAP with RNAi to remove YAP-HaloTag/YAP within these cells resulted in no anti-YAP labeled condensates (Figs. 3g, h).

We next examined YAP localization in cells within mouse kidney, a tissue known to experience hyperosmotic stress, with kidney medulla cells experiencing a more

hyperosmotic environment than cortical cells[22-25] (Fig. 3i). YAP antibody localization in cortical kidney cells was restricted primarily to the cytoplasm (Fig. 3j, top; Fig. 3k), with few if any nuclear puncta seen (Figs. 3j, top; Fig. 3l). By contrast, YAP in medulla cells was enriched in the nucleus (Fig. 3j, bottom; Fig. 3k) and contained prominent punctate structures that resembled YAP nuclear condensates seen in osmotically-stressed HEK293T and U-2 OS cells (Figs. 3j, bottom; Fig. 3l).

Characterizing cytoplasmic YAP condensates induced by hyperosmotic stress.

We found that YAP cytoplasmic condensates concentrated proteins involved in YAP-specific post-translational modifications, including Hippo pathway kinase large tumor suppressor 1 (LATS1) (Fig. 4a) and Nemo-like kinase (NLK) (Fig. 4b). Since prior work has shown that hyperosmotic stress leads to activation of both NLK and LATS1/2[6], these findings raised the possibility that localization of NLK and LATS1/2 within cytoplasmic YAP condensates might coordinate the activity of both kinases.

LATS1/2 is known to phosphorylate YAP at Ser127, causing it to become more tightly associated with 14-3-3 proteins and retained in the cytoplasm[26,27]. Because there was less mCherry-YAP localized in the nucleus in EGFP-LATS1 overexpressing cells compared to cells not expressing EGFP-LATS1 after sorbitol treatment (compare Fig. 4a and Fig. 2c), the data suggested that enhanced phosphorylation of YAP at Ser127 helps retain YAP in the cytoplasm in EGFP-LATS1 overexpressing cells. Consistent with this, mutating serine 127 to alanine in YAP (to prevent phosphorylation by LATS) significantly increased YAP's nuclear localization during hyperosmotic shock (Fig. 4d).

NLK phosphorylates YAP at Ser128, releasing YAP from binding to 14-3-3 proteins to allow YAP nuclear import[6,28]. To test whether phosphorylation of YAP at Ser128 in cytoplasmic droplets helps promote YAP's nuclear redistribution in NLK-expressing cells, we mutated serine 128 to alanine in YAP. We found this significantly impaired YAP's ability to become nuclear-localized in response to hyperosmotic shock (Fig. 4d), without impairing its ability to form droplets (Fig. 4c).

YAP cytoplasmic droplets did not contain the stress granule component G3BP (Fig. 4e) nor did they co-segregate with G3BP-containing stress granules during arsenite treatment (Fig. 4f). They also were not processing bodies (P-bodies) involved in RNA processing as they lacked critical P-body components, including GW182 and Ago2 (Extended Data Figs. 4a-d). However, the P-body component Dcp1a did co-segregate with YAP droplets (Figs. 4g), suggesting some unknown link to RNA processing. Altogether, the data revealed that YAP cytoplasmic condensates are neither stress granules nor P-bodies, but are a type of cytoplasmic droplet that sequesters kinases that target YAP for either cytoplasmic retention or nuclear translocation.

Characterizing nuclear YAP condensates induced by hyperosmotic stress

YAP nuclear condensates did not co-localize with known nuclear body markers such as PML (promyelocytic leukemia bodies, Figs. 5a, b) or Coilin (Cajal bodies, Figs. 5c, d), suggesting they perform functions different from these well-known nuclear bodies. Instead, YAP condensates were enriched in the transcription factor TEAD1 (Figs. 5e, f), which regulates

transcription of YAP target genes[1,29,30]. Neither YAP nor TEAD1 were found in nuclear or cytoplasmic droplets prior to sorbitol treatment. Within 2 min of hypertonic stress, however, both molecules were found co-localized in nuclear condensates. Line scans through the condensates showed a similar profile of enrichment for each protein in the droplet (Fig. 5f). A similar co-localization of YAP and TEAD1 in droplets was seen in U-2 OS cells in response to hyperosmotic stress induced by PEG (Extended Data Figs. 5a, b).

YAP nuclear condensates also contained the paralog of YAP, WW domain containing transcription regulator (TAZ) (Figs. 5g, h), which recently has been reported in nuclear phase condensates[31]. In HEK293T cells, TAZ and YAP both were homogenously dispersed in the cytoplasm prior to hyperosmotic treatment, but redistributed into nuclear droplets within 20 sec of treatment (Fig. 5g). In the droplets, YAP and TAZ showed similar overall distributions (Fig. 5h). Co-expressing EGP-TAZ and mCherry-YAP in U-2 OS cells, revealed the two molecules were co-localized in the same droplets after hyperosmotic stress (Extended Data Fig. 5c). Observing the same cell before and after hyperosmotic treatment revealed mCherry-YAP redistributed into pre-existing EGFP-TAZ droplets, as well as into new ones, into which EGFP-TAZ later redistributed (Extended Data Fig. 5c).

3D ATAC PALM reveals YAP nuclear condensates localize to spatially-segregated accessible chromatin domains

The linear distribution of chromatin accessible for binding by transcription factors, promoters and insulators has been mapped by DNase I digestion[32,33] and by assay for transposase-accessible chromatin with high-throughput sequences (ATAC-seq)[34], revealing that many gene enhancer elements cluster with their transcription factors into super-enhancer (SE) regions. Given that nuclear YAP condensates were enriched in YAP-specific transcription factors and coactivators, we asked whether these condensates marked SE regions. To test this, we visualized accessible chromatin in cells using a recently developed ATAC-based imaging method called 3D ATAC photoactivated localization microscopy (ATAC-PALM)[35]. In this approach, Tn5 transposase is used to insert photo-activatable fluorescent DNA probes into the accessible chromatin domains (Fig. 6a, left), and then photoactivated localization microscopy (PALM)[36] combined with Lattice Light Sheet microscopy (LLSM)[37,38] is employed to visualize accessible chromatin regions in 3D through the entire nucleus (Fig. 6a, right).

Prior to hyperosmotic shock, ATAC-PALM imaging revealed that accessible-chromatin regions were widely dispersed throughout the nucleus with a few of these regions clustered into observable puncta (Fig. 6b, arrows, Movie S5). Strikingly, after 5 min of hyperosmotic treatment with sorbitol, large ATAC-labeled clusters were seen distributed across the nucleus (Fig. 6c, arrows, Movie S6). Pair autocorrelation analysis, used to quantify differences in the density and size of the clustered accessible-chromatin regions, revealed that accessible-chromatin regions under sorbitol treatment, on average, became significantly more clustered than before treatment (Fig. 6d). Measurement of the radius of the ATAC clusters in sorbitol-treated cells demonstrated that some clusters were over 400 nm in diameter, significantly larger than those in control cells, whose average diameter was ~120 nm (Fig. 6e). The significant size increase in ATAC-labeled clusters could reflect fusion of neighboring

accessible chromatin regions, the appearance of entirely new accessible-chromatin regions, or both.

To test whether the enlarged ATAC-positive structures under sorbitol treatment represented YAP condensates, we compared the localizations of ATAC structures with EGFP-YAP condensates in sorbitol-treated cells. Remarkably, virtually all ATAC-positive structures were associated with the EGFP-YAP condensates (Fig. 6f, Movie S7). This suggested that osmotically-driven phase separation of YAP into condensates reorganizes the genome into clusters of accessible chromatin regions enriched in YAP and its binding partners.

Nuclear YAP condensates become sites of active gene transcription

To determine whether nuclear YAP condensates with accessible chromatin domains are sites of active gene transcription, we probed them with antibodies to RNA Polymerase II (RNAPII). RNAPII was initially segregated from YAP nuclear droplets at 10 min of hyperosmotic shock using sorbitol (Figs. 7a, b; Extended Data Fig. 6a). However, after 2 h in sorbitol RNAPII was no longer excluded from YAP condensates. Instead, RNAPII now decorated the surface of nuclear YAP condensates (Fig. 7c, Extended Data Fig. 6b). This suggested that YAP nuclear condensates, while initially driving clustering of gene enhancer elements to form SEs, do not recruit RNAPII until later, presumably after the cell has had time to adapt to hyperosmotic conditions for reorganization of its transcription program.

Given that RNAPII localizes to the surface of YAP condensates by 2 h of hyperosmotic stress, we examined the distribution of nascent RNA to determine whether the condensate sites were active for gene transcription. Nascent RNA did not specifically localize at clustered sites before treatment or at YAP-containing nuclear condensates after 5 min sorbitol treatment (Figs. 7d, e). However, 2 h after cells were in sorbitol, a large amount of nascent RNA was transcribed selectively at clustered sites associated with nuclear YAP condensates (Fig. 7f). That this leads to an increase of YAP target gene transcription was suggested by RT-PCR experiments, which showed an increase in expression of the YAP target gene products Ctgf and Cyr61 within 3 h of sorbitol treatment (Fig. 2a).

YAP's intrinsically-disordered transcription activation domain is responsible for YAP condensate formation and its downstream effects on transcription

To test whether YAP droplet formation is necessary for the above effects on gene transcription, we deleted the intrinsically-disordered C-terminal transcriptional activation domain (TAD) of YAP (generating EGFP-YAPΔTAD) (Fig. 8a). Upon expression of EGFP-YAPΔTAD, only ~2.3% of the expressing cells formed condensates upon hyperosmotic shock, compared to ~92.7% of cells expressing EGFP-YAP (Fig. 8b). This suggested that without its TAD sequence YAP is unable to phase separate into condensates. Notably, endogenous YAP failed to form condensates in cells expressing EGFP-YAPΔTAD (Extended Data Fig. 7b-c), suggesting the mutant could act as a dominant negative in YAP phase condensation.

In EGFP-YAPΔTAD expressing cells, in which YAP condensates didn't form, TEAD1 did not enrich in any nuclear foci upon hyperosmotic stress (Fig. 8c). Measuring Ctgf and Cyr61 mRNA expression 3 h after sorbitol treatment revealed a significant decrease in expression

of the mRNAs in cells expressing EGFP-YAPΔTAD compared to cells expressing EGFP-YAP (Fig. 8d). These results suggested that YAP's intrinsically-disordered transcription activation domain is responsible for YAP condensate formation and later expression of YAP target genes during sorbitol treatment.

Discussion

Our work shows that nuclear localization and activity of YAP, a key Hippo pathway transducer, is regulated by liquid-liquid phase separation. Specifically, hyperosmotic stress-induced condensation of YAP into liquid droplets shifts YAP's distribution from cytoplasm to nucleus, where it drives transcription of genes involved in cell proliferation. Because cytoplasmic and nuclear YAP droplets sequestered different sets of proteins, with cytoplasmic droplets containing NLK and nuclear droplets containing TEAD1, their formation appeared to contribute both to YAP's ability to redistribute into the nucleus and to its role in transcriptional control. Our findings thus highlight a mechanism involving phase separation that enables YAP to collaborate with different factors in different cellular compartments to control its activity during signaling.

The Hippo signaling pathway governs tissue growth and homeostasis by regulating cell proliferation and differentiation, with control of these cellular processes occurring through pathway-mediated localization of the downstream effectors YAP/TAZ. The overall activity of Hippo signaling is to prevent the transcriptional activity of downstream effectors of YAP and TAZ, accomplished by retention of these transcription co-factors in the cytoplasm through the activity of a cascade of core kinases (including the kinases MST1/2 and Lats1/2). While many signals activate the Hippo pathway (i.e., by engagement of receptors that activate the core kinases), the events that antagonize the pathway have only begun to be understood. One antagonizing event is phosphorylation of YAP at Ser 128 by NLK, which occurs in response to hyperosmotic stress and leads to YAP redistribution into the nucleus[6]. Our finding that NLK co-localizes with YAP in cytoplasmic droplets under hyperosmotic stress suggests this co-compartmentalization serves to rapidly alter YAP phosphorylation kinetics through increased kinase- and substrate- concentrations in the droplet. The additional presence of Lats1 in YAP cytoplasmic droplets could serve to modulate this effect, as we observed decreased pools of YAP in the nucleus in Lats1 overexpressing cells. YAP sequestration into cytoplasmic condensates under hyperosmotic stress could help prevent YAP from interacting with 14-3-3 proteins, such as 14-3-3σ protein. In addition, cytoplasmic YAP condensates could also protect YAP from targeted degradation by phosphorylated casein kinase in the cytoplasm[39]. Understanding how these and other core Hippo kinase members, including MST1/2, PP2A, Sav1 and MOB1, distribute and behave when YAP droplets form under hyperosmotic stress is an important area for future work as their modulation could be relevant in therapeutic studies.

Another area impacted by our findings relates to nuclear reorganization by YAP condensates. A growing body of work that includes light-induced phase-separation systems[40-42] has suggested the importance of phase separation in re-organizing the genome for transcription[12-15]. Our finding of osmotically-driven assembly and later disassembly of YAP nuclear condensates provides a, physiologically relevant approach for analyzing

condensate-induced changes in nuclear organization. Indeed, using the super-resolution imaging method of ATAC-PALM to visualize accessible chromatin regions, we found that the cell's genome reorganized dramatically within 5 min of hyperosmotic stress. During this interval, dispersed accessible chromatin domains observed in untreated cells became highly concentrated in large, YAP-containing nuclear condensates.

Canonically, YAP binds to TEAD family members to induce transcription of YAP target genes. But how the targeted genomic loci are coordinately controlled has been unclear. YAP constructs incapable of condensate formation (i.e., YAPΔTAD) prevented both TEAD1 localization to clusters and YAP target gene expression during hyperosmotic stress, suggesting the presence of YAP condensates during hyperosmotic stress is functionally relevant for YAP signaling. We found TEAD1, TAZ and accessible chromatin regions co-localize with newly formed YAP droplets within minutes of hyperosmotic stress. This raises the possibility that YAP nuclear condensates physically pull in targeted genomic loci while pushing out non-targeted regions of neighboring genome to allow for synchronized transcription of YAP target genes, a characteristic of nuclear condensates proposed by others[12,13,15,41]. During this genome reorganization, we observed that while RNAPII was initially excluded from the YAP droplets, it later became localized to the rim of the droplets, as did newly transcribed RNA. This coincided in time with the expression of YAP downstream target genes in these cells. Therefore, YAP nuclear condensates dynamically restructure the overall genomic environment over time (Fig. 8e).

In summary, we've shown that YAP's distinct localizations/functions in cytoplasm and nucleus can be controlled by its ability to undergo phase condensation in response to hyperosmotic stress. This allows YAP to be a sensor of mechanical forces in tissues that cause changes in macromolecular crowding. Additional strategies for modifying YAP target gene expression may thus become possible for altering the course of cancer and other diseases involving YAP signaling, for example, through droplet disrupters or reagents that change macromolecular crowding.

1. Material and Methods

Constructs

pEGFP-C3-hYAP1 (Addgene #17843) and pEGFP C3-Mst2 (Addgene #19056) were gifts from Marius Sudol. mCherry-Dcp1a was a gift from Pick-Wei Lau. mCherry-NLK construction: PCR-amplify NLK from pDONR223-NLK (gift from William Hahn & David Root, Addgene #23642) with 5'- ctcaagcttcgaattctgcaCTTCCACACCTCCCTCCTC-3' and 5'- gatccggtggatcccgggccCTCCCACACCAGAGGAGATG-3'; PCR-amplify pmCherry-C1 (Clonetech) with 5'- GGCCCGGGATCCACCGGA-3' and 5'- TGCAGAATTCGAAGCTTGAGCTC-3'. Assemble amplified NLK and mCherry-C1 with NEBuilder HiFi DNA Assembly Master Mix. pET28b-EGFP-YAP construction: pET28b (+) (EMDMillipore) and pEGFP-C3-hYAP1 are each double-digested with NheI and EcoRI (NEB) and ligated together by T4 DNA Ligase. Subsequently, EGFP-YAP is brought in-frame with 6xHis-thrombin by QuikChange Lightning Site-Directed Mutagenesis Kit (Agilent 210519) by primers: 5'- gctaccggtcgccacatggtgagcaagg-3' and 5'- ccttgctcaccatgtggcgaccggtagc-3'. For generation of YAP truncations, pEGFP-C3-hYAP1

(addgene # 17843) was used as template to amplify YAP-ΔP (FWR 5'- GGAAGATCTTCC CAT CAG ATC GTG CAC GTC CG-3' and REV 5'- CCGGAATTCCGG CTA TAA CCA TGT AAG AAA GCT TTC TTT ATC −3') and YAP-ΔTAD (FWR 5'- GGAAGATCTTCC ATG GAT CCC GGG CAG CAG −3' and REV 5'- CCGGAATTCCGG CTA ACC CAT GAC GCC TCC CTG −3') by PCR and then these were cloned into Bgl II/EcoRI sites of pEGFP-C3. To generate pEGFP-YAP-S127A, pEGFP-YAP-S128A constructs, pEGFP-C3-hYAP1 construct is used as template, and QuikChange Lightning Site-Directed Mutagenesis Kit is used to make point mutations using primers: 5'-gagaagctggagaggcatgagctcgaacatgct-3' (forward) and 5'-agcatgttcgagctcatgcctctccagcttctc-3' (reverse) for S127A, and 5'-gttcgagctcattccgctccagcttctctgcAGT-3' (forward), 5'-gcagagaagctggagcggaatgagctcgaacATGCT-3' (reverse) for S128A.

In vitro EGFP-YAP expression, protein purification, and phase separation experiments

pET28b-EGFP-YAP was used to transform E.Coli BL21 DE3 RIPL cells (Invitrogen) using standard supplier protocol. Cells were grown to OD 0.6, lyzed using a tip sonicator, and purified using His-tag affinity chromatography on a GE-Healthcare AKTA system. The purified protein was concentrated to ~ 1 mg/mL and run on a Sephadex 200 size exclusion column in 20 mM Tris pH 8.0. The collected fractions contained the clean protein, as verified with SDS PAGE and MALDI-TOF mass spectrometry. Phase separation conditions were assessed by sample turbidity, measured through the OD at 600 nm of EGFP-YAP solutions in 96-well clear-plastic plates using a Molecular Designs SpectraMax plate reader. To determine the partition coefficient, K_P of YAP (Fig. 3I) between solution and protein-rich droplets, phase separation reactions were prepared in 1.5 mL tubes with 40 μM EGFP-YAP, and different PEG sizes in concentrations ranging from 0 to 35 wt% (Sigma), and 20 mM Tris buffer pH 8.0. At given times, the reaction solution was gently stirred, and a 50 μL aliquot was removed. The aliquot was spun down at max speed for 15 minutes. A bright green pellet was observed on the bottom of the tubes, and the supernatant was carefully removed, diluted 5x in tris buffer, and placed in a 96-well plate for absorbance measurements at the maximal absorbance wavelength of EGFP, 488 nm. The concentration of EGFP-YAP in the soluble phase was estimated based on EGFP absorbance.

Confocal imaging of purified EGFP-YAP was done on an LSM-880 equipped with an Ar laser line. Imaging chambers were prepared on clean glass slides using a 120 μm double-sided sticker (Grace Biolabs), and sealed with a 1.5 coverslip. Imaging was done on a single slice, with the pinhole opened to 2 Airy units.

Cell Culture, Transfection, siRNA and Live-cell imaging

U-2 OS (gift from Lingfeng Chen) and HEK293T (gift from Anirban Banerjee Lab) cells are cultured in complete medium: Dulbecco's modified Eagle's medium (DMEM) supplemented with 10% fetal bovine serum (FBS) (Gibco), 100 units/ml penicillin/streptomycin (Corning), and 2mM L-glutamine (Corning) at 37°C and 5% CO2. No ICLAC cell lines have been used in this study. For confocal imaging, cells are cultured on 8-well LabTek chambered coverglass dishes (Thermo Scientific), and transfected with Lipofectamine 3000 Reagent (Thermo Fisher). Cells are imaged 18hrs after transfection on a

Zeiss LSM780 confocal microscope at room temperature with Plan-Apochromat 63x/1.40 Oil objective. For RNAi experiments, YAP siRNA (Thermo Fisher Silencer Select s20367) or negative control (Thermo Fisher AM4611) is transfected into cells (pre-seeded on 6-well plate) using Lipofectamine™ RNAiMAX Transfection Reagent (Thermo Fisher 13778075). 48 hr after transfection, cells are replated onto 6-well plates for confirming knock down by immunoblotting, or to 8-well LabTek chambered coverglass dishes for imaging on the following day. Images are taken every 30 sec, in a z-stack of 3 slices with an interval of 0.4μm. For volume measurements, cells pre-transfected with EGFP-YAP are labelled with Hoechst 33342 (Thermo Fisher 62249) for 30 min prior to confocal imaging. Dual color imaging and z-sectioning is done across the whole cell and nuclear volume, with an interval of 0.5μm. Cell and nuclear volume measurements are done with Imaris software (Bitplane) using surface reconstruction tool, and cytoplasmic volume is calculated by substracting cell volume (EGFP channel) with nuclear volume (Hoechst channel). To visualize fusion of YAP condensates, images are taken every 4.5 sec with Definite Focus. Zoomed-up images are smoothened once using ImageJ for display.

Fluorescence Recovery after Photobleaching (FRAP)

HEK293T cells expressing EGFP-YAP is treated with 0.2M sorbitol, and FRAP experiments are done on cytoplasmic or nuclear YAP condensates formed immediately after treatment using Bleaching mode in Zen. Region of interest is selected on either the entire condensate or part of it using a rectangular box of approximately 1μm x 1μm in size. 20 iterations of bleaching are done with 100% 488nm Argon laser. 5 rounds of imaging are done prior to, and 300 rounds of imaging are done after bleaching until fluorescence signal plateau, with an interval of 450 msec. $t_{1/2}$ is calculated with FRAP module in Zen software, using fit formula for 1 diffusion component.

RT-PCR

HEK293T cells are serum-starved for 1hr, and subject to control serum-free medium or 0.2M sorbitol serum-free medium, according to methods described in Hong et. al[6]. Total RNA is isolated from HEK293T cells using Qiagen RNeasy mini kit (Qiagen 74104) and converted to cDNA with Thermo Fisher High-Capacity cDNA Reverse Transcription Kit (Thermo Fisher 4368814). RT-PCR is carried on an Agilent AriaMx 96 Real-Time PCR System, with Platinum SYBR Green qPCR Supermix-UDG (Thermo Fisher 11733038). The following primers are used: Gapdh: 5’-CTCCTGCACCACCAACTGCT-3’ (forward), 5’-GGGCCATCCACAGTCTTCTG-3’ (reverse). Ctgf: 5’-AGGAGTGGGTGTGTGACGA-3’ (forward), 5’-CCAGGCAGTTGGCTCTAATC-3’ (reverse). Cyr61: 5’-CCTCGGCTGGTCAAAGTTAC-3’ (forward), 5’-TTTCTCGTCAACTCCACCTC-3’ (reverse). mRNA levels are normalized to that of Gapdh.

Generation of YAP-HaloTag CRISPR knock-in U-2 OS cell line

Singe-guide RNA (sgRNA) targeting +/− 100bps around the stop codon of Yap gene was designed using the web-based CRISPR design tool (http://crispr.mit.edu). One guide is chosen due to its spanning the stop codon and high score: tacatggttatagagccctc. DNA oligonucleotides with BbsI restriction sites are ordered from Integrated DNA Technologies (IDT). pSpCas9(BB)-2A-GFP (PX458) vector (Addgene 48138, a gift from Feng Zhang)[43]

was digested using BbsI and ligated with annealed gRNA fragment to form Yap gRNA-Cas9 plasmid.

The homology repair fragment spanning Yap stop codon (~800bp on each side) and containing Halo protein-coding gene is synthesized with gBlock IDT. The gBlock sequence is included in Supplementary Note 2. pUC57-mini vector (GenScript) is linearized with EcoRV restriction enzyme, and ligated with Halo homology repair fragment using NEBuilder® HiFi DNA Assembly Master Mix (NEB E2621). All plasmids are sequence-verified by Eurofins Genomics.

Yap gRNA-Cas9 and Halo homology repair constructs are co-transfected into U-2 OS cells with Lipofectamine 3000 Transfection Reagent (Thermo Fisher L3000015). 48 h after transfection, GFP-positive cells are selected using fluorescence-activated cell sorting (FACS, National Eye Institute Flow Cytometry Core). Cells are grown for an additional week, and stained by 100nM JF549 Halo dye (gift of Luke Lavis, HHMI Janelia Research Campus) for 30 min, washed 3 times with 1xPBS, and FACS-sorted for a second time for Halo dye-positive and GFP-negative cells. Individual cells are grown in single wells of a 96-well dish supplemented with 20% FBS DMEM medium, and waited for 1 week for positive clones to form. Cell clones are seen in 40% of the wells. Correct genome insertion is verified by genome DNA extraction (QuickExtract™ DNA Extraction Solution, Lucigen QE09050), and PCR using primers spanning homology arms and Halo tag: 5'-attcctgggacaaatgtggaccttg-3' (forward), 5'-tcaggtctggagcaatgcagcgatg-3' (reverse); and 5'-tgaatcctgttgaccgcgagccactg-3' (forward), 5'-tagaattcagtctgcctgagggctc-3' (reverse). Increased protein size of YAP marked by Halo is further confirmed by immunoblotting with anti-YAP antibody (Cell Signaling 14074S, 1:150).

Live-cell imaging of U-2 OS YAP-HaloTag cell line

YAP-HaloTag U-2 OS cells are pre-plated on 8-well LabTek chambered coverglass dishes for at least 16 hrs in complete medium. Prior to imaging, incubate cells with complete medium containing 100 nM JF549 Halo dye for 30 min, and then wash 3 times with 1x PBS medium before changing back to complete medium. Complete medium and 1x PBS need to be isotonic (no old medium with water evaporated) to prevent early formation of YAP-HaloTag condensates. Imaging is done on a Zeiss LSM880 scope with Airyscan (Superresolution mode), using a Plan-Apochromat 63x/1.4 oil DIC M27 objective. RFP 561nm laser is used to excite the Halo dye, and is kept under 0.7% power to minimize photobleaching. Pinhole is kept at 132 μm, and pixel sizes are 35 nm x 35 nm.

Mice

Eight-weeks female (FVB/NJ) mice were purchased from The Jackson Laboratory (https://www.jax.org) and housed at the National Institutes of Health (NIH)/ National Cancer Institute (NCI) mice facility 10/ACRF in accordance with NIH/NCI regulations for the use of mice in experimental research. All procedures were performed according to protocols (LCMB-037) approved by the veterinary authorities at NIH/NCI. The study is compliant with all relevant ethical regulations regarding animal research.

Kidney dissection and Immunofluorescence

Kidney tissue from 2 WT mice were immersion-fixed with 4% PFA in phosphate buffered saline (PBS) for 48 hr at 4 °C. For immunofluorescence microscopy (IF) stainings, fixed kidney tissue was mounted in 5 % low melting agarose in PBS and sectioned into 75 μm thick slices using a vibratome (Leica). Floating sections were permeabilized in 0.5 % Triton-X100 in PBS for 1 hr, and blocked by incubation with blocking buffer (20% FBS + 0.2 % Triton-X100 in PBS) for 2 hr. Sections were incubated sequentially with a primary antibody against YAP (1:50) (Cell Signaling) in blocking buffer for 72hrs, washed 6 times for 10 min with 0.2 % Triton-X100 in PBS, incubated with secondary antibody labelled with Alexa fluorophore 488 (1:500), Hoechst (1:5000) and Alexa fluorophore 568-conjugated Phalloidin (1:150) in blocking buffer overnight, and washed again with 0.2% Triton-X100 in PBS 6 times for 10 min. Stained sections were incubated in 50% glycerol overnight, and then mounted in slides in 80% glycerol. Fixed kidney samples were imaged with a Leica SP8 laser scanning confocal microscope (DMI8-CS) using a 63× 1.4 oil objective, 405, 488 and 552 laser lines and HyD detectors. Images of the kidney cortex and medulla were acquired.

Immunofluorescence and Nascent RNA Pulse Labeling

HEK293T cells are plated on coverslips precoated with fibronectin (7.5μg/ml, Millipore, FC010) for 16 h, before being fixed with 4% paraformaldehyde (PFA, EMS), permeabilized with 0.5% TritonX-100, and blocked with 3% BSA in 1xPBS. Incubate with primary antibodies in 1% BSA overnight at 4°C, and then incubate with Alexa Fluor-conjugated secondary antibodies. The following primary antibodies are used: anti-YAP (Cell Signaling 14074S, Lot 4, 1:150); anti-TEAD1 (BD Biosciences 610922, Lot 6228876, 1:200); anti-RNA polymerase II CTD repeat YSPTSPS (phospho S2) (Abcam ab193468, 1:150); anti-G3BP1 (proteintech 13057-2-AP, 1:5000); anti-PML (Abcam ab96051, Lot GR3174201-1, 1:500); and anti-Coilin (Abcam ab87913, Lot GR50257-4, 1:200). Nascent RNA is labelled using Click-iT™ RNA Alexa Fluor™ 594 Imaging Kit (Thermo Fisher C10330). All samples are transiently labelled with 2.5mM 5-ethynyl uridine (EU) for 5 min prior to fixation with 4% PFA. Specifically, sample treated with 5 min sorbitol is supplemented with 0.2M sorbitol with 2.5mM EU for 5 min. Sample treated with 2 h sorbitol is supplemented with 0.2M sorbitol for 1 h 55 min before changing to 0.2M sorbitol supplemented with 2.5mM EU and incubated for 5 min. Each sample is incubated with GFP-Booster_Atto488 (ChromoTek gba488-100) after fixation and permeabilization, before performing Click chemistry to visualize EU following the manufacturer instructions. For imaging and quantification, at least 15 fields of view per coverslip are randomly chosen by Hoechst nuclear staining and imaged by Zeiss LSM780, LSM880 confocal microscope or Airysan. At least 3 different coverslips are quantified per treatment type.

Colocalization

Colocalization of two channels are done with ImageJ Coloc 2 plugin. ROI is chosen on the either the cytoplasm or the nucleus. Pearson’s R value is used for measuring colocalization of two channels.

3D ATAC-PALM imaging:

Sample preparation for 3D ATAC-PALM imaging

We prepared samples for 3D ATAC-PALM experiments as reported previously[35,44]. HEK293 cells were plated onto 5mm coverslips (Warner Instruments, cat#64-0700) at around 80% confluency with proper coating one day before experiment. Control cells or cells under 5 min sorbitol treatment were fixed with 4% paraformaldehyde (Electron Microscopy Sciences, Cat# 15710) for 10 min at room temperature. After fixation, cells were washed three times in 1×PBS for 5 minutes and then permeabilized in ATAC lysis buffer (10 mM Tris–Cl, pH 7.4, 10 mM NaCl, 3 mM MgCl2, 0.1% Igepal CA-630) for 10 min at room temperature. After permeabilization, the coverslips were washed twice in 1×PBS. The transposase mixture solution was prepared according to previous research[44] and was added to the cells. The sample was incubated in a humidity chamber box for 30 min at 37 °C. After incubation, the coverslips were washed three times with 1×PBS containing 0.01% SDS and 50 mM EDTA for 15 min at 55 °C before mounted onto the Lattice light-sheet microscope (LLSM) slot for 3D ATAC-PALM imaging.

3D ATAC-PALM image acquisition and processing

The 3D ATAC-PALM imaging was performed following published procedures[44] by using the lattice light-sheet microscopy[37]. The light sheet was generated from the interference of highly parallel beams in a square lattice and dithered to create a uniform excitation sheet. The inner and outer numerical apertures of the excitation sheet were set to be 0.44 and 0.55 during experiments, respectively. In order to maintain stable imaging conditions in particular constant salt concentration, a Variable-Flow Peristaltic Pump (Thermo Fisher Scientific) was used to connect a 2L reservoir with the imaging chamber with 1×PBS circulating through at a constant flow rate. Labelled cells were placed into the imaging chamber and each image volume includes 100~200 image frames. Initially, fluorescent PA-JF_{549} dye were pushed into the dark state through repeated photo-bleaching by maximal laser power (2W) (MPB Communications Inc., Canada). The samples were then imaged by iteratively photo-activating each focal plane with very weak intensity 405 nm light (<0.05 mW power at the rear aperture of the excitation objective and 6W/cm^2 power at the sample) for 8 ms, followed by exciting each plane with a 2W 560 nm laser at its full power (26 mW power at the rear aperture of the excitation objective and 3466 W/cm^2 power at the sample) for 20 ms exposure time. The specimen was illuminated when laser light went through a custom 0.65 NA excitation objective (Special Optics, Wharton, NJ) and the fluorescence generated within the specimen was collected by a detection objective (CFI Apo LWD 25×W, 1.1 NA, Nikon), filtered through a 440/521/607/700 nm BrightLine quad-band bandpass filter (Semrock) and N-BK7 Mounted Plano-Convex Round cylindrical lens (f = 1000 mm, Ø 1”, Thorlabs), and eventually recorded by an ORCA-Flash 4.0 sCMOS camera (Hamamatsu).

We embedded nano-gold fiducials within the coverslips for drift correction during imaging process as previously described[38]. ATAC-PALM Images were taken to construct a 3D volume when the sample was moving along the sample axis. Individual volumes per acquisition were automatically stored as Tiff stacks, which were then analyzed by in-house scripts written in Matlab. The cylindrical lens introduced astigmatism in the detection path

and recorded each isolated single molecule with its ellipticity, thereby encoding the 3D position of each molecule relative to the microscope focal plane. The localization precision was estimated to be 26±3 nm and 53±5 nm for xy and z respectively by calculating the standard deviation of all the localizations coordinates (x, y and z) after the nano-gold fiducial correction.

Equations processing raw ATAC-PALM data is included in the Supplementary Note 1.

DBSCAN analysis

The DBSCAN algorithm (Density-Based Spatial Clustering of Applications with Noise) was adopted to map and visualize individual local ACDs (core DBSCAN Matlab code from http://yarpiz.com/255/ypml110-dbscan-clustering). The algorithm first finds neighboring data points within a sphere of radius *r*, and adds them into same group. In parallel, a predefined threshold minimal points (*minPts*) was used by the algorithm to justify whether any counted group is a cluster. If the number of points within a group is less than the threshold *minPts*, the data point is classified as noise. We implemented DBSCAN analysis on the localization data for both the control and 5min sorbitol-treated cells by using 150 nm as the searching radius (*r*) (peak radius from the Ripley's H function analysis) and empirically setting *minPts* as 10. To reconstruct the *iso*-surface for each identified accessible chromatin cluster, the convex hull of each accessible chromatin cluster was calculated and visualized by using Matlab. The volume of the convex hull was computed, and the normalized cluster radius (calculated from a sphere with equal volume) was calculated and shown in violin plot.

Code availability

Software for identifying, localizing and plotting single-molecule data is freely available after execution of a research license with HHMI. The software for G(r) and DBscan analysis is freely available from https://github.com/ammondongp/3D_ATAC_PALM

Data availability

Source data for Figs. 2-8 has been provided as Source Data Figure 2-8. Source data for Extended Data Figs. 1-5 and 7 has been provided as Source Data Extended Data Figures 1-5 and 7. All other data supporting the findings of this study are available from the corresponding author on reasonable request.

Statistics and Reproducibility

No statistical methods were used to predetermine sample sizes. Some experiments were randomised and the investigators were blinded to allocation during experiments and outcome assessment. At least 20 images are taken for each experiment involving live-cell imaging or immunofluorescence, and 3 repeats are performed for each experiment. The sample size is sufficient since we usually detect large difference between two experimental conditions, with p-value lower than 0.01.

All quantitative data shown represent means ± SEM. Bar plots have been overlaid with dot plots showing all individual data points measured.

No outlier suggestions were computed. No strongly scattering data points were excluded, but all quantitative evaluation data points were taken into account and averaged to fully represent biological and technical variabilities.

Statistical analyses were done using GraphPad Prism software. Statistical significance calculations comparing two conditions were done using two-tailed unpaired t-test (normal data distribution), two-tailed paired t-test, or Mann-Whitney U-test.

The experiments are repeated at least three times and are reproducible.

Extended Data

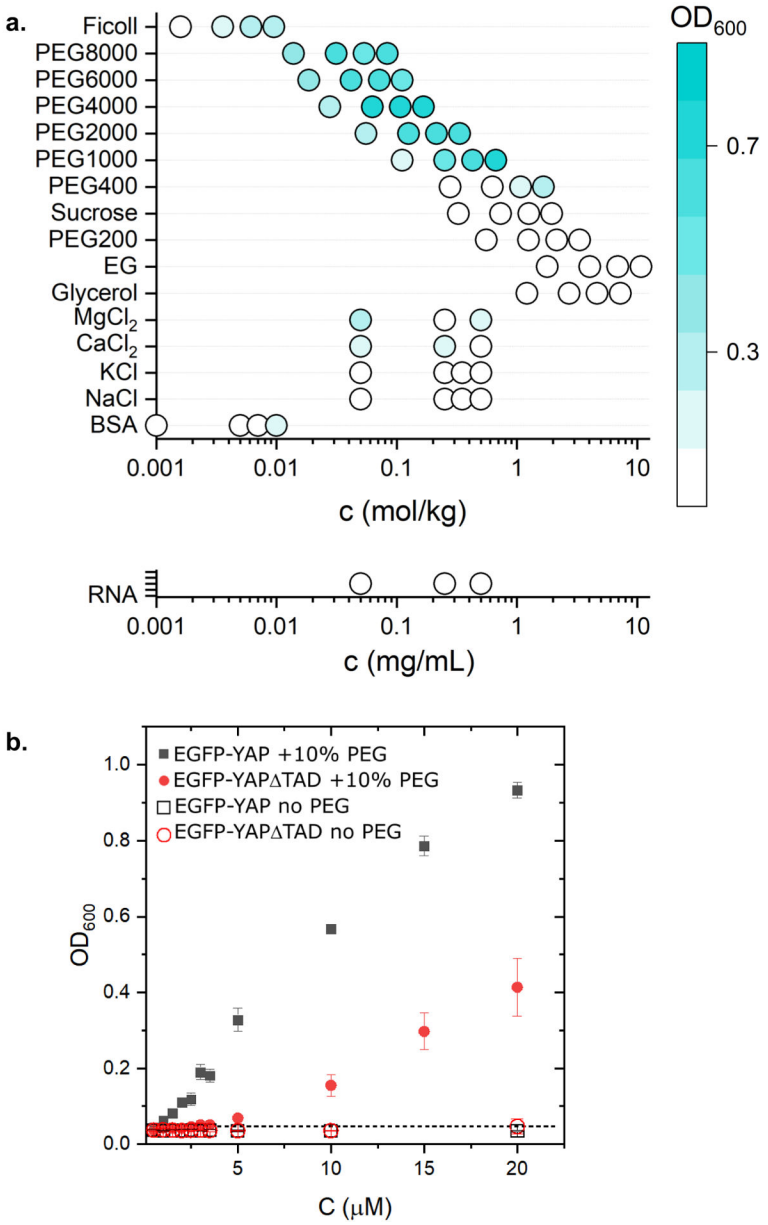

Extended Data Fig. 1. More characterizations of recombinant YAP protein in vitro.

(a) Turbidity measurements of purified EGFP-YAP at different salt, BSA and RNA concentrations. The experiment has been repeated 3 times independently with similar results. (b) In vitro turbidity assay showing purified EGFP-YAP phase separates at much lower concentrations than EGFP-YAPΔTAD in the presence of 10% PEG2000. Error bars are SD from three repeats. Center of the data is mean. n=3 biologically independent experiments. Statistics source data are provided in Source Data Extended Data Figure 1

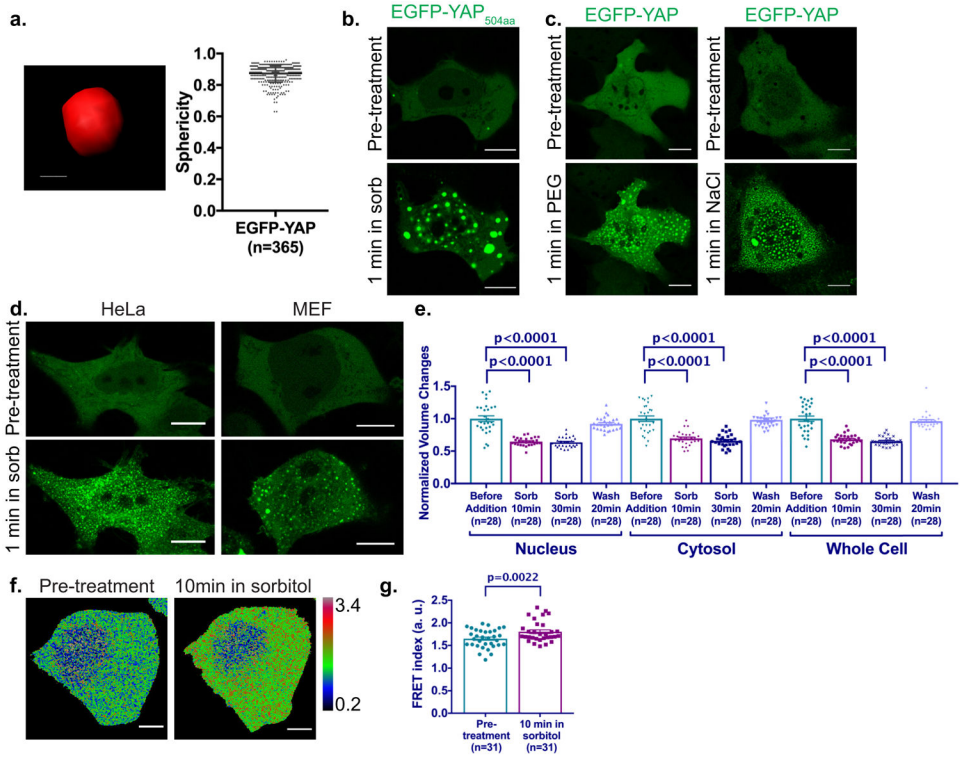

Extended Data Fig. 2. EGFP-YAP condensates form in hyperosmotic stress.

(a) Imaris 3-D rendering of an EGFP-YAP condensate, and quantification of sphericity of those condensates using Imaris. Center of the data is mean. Error bars are SD. Scale bar: 0.5μm. (b-d) Live-cell imaging of EGFP-YAP in HEK293T cells showing nuclear and cytoplasmic condensates are able to form with different isoforms of YAP (b) and in different hyperosmotic agents (c). (d) Live-cell imaging showing different cell types are able to form EGFP-YAP condensates under hyperosmotic stress. Scale bars are 10μm. All the experiments are repeated 3 times independently with similar results. (e) Quantification of normalized HEK293T nuclear, cytosolic and total volume before and after sorbitol treatment, and after wash. Center of the data is mean. Error bars are SEM. Two-sided paired t-test. Comparing to volume before treatment. Error bars show SEM. n=28 biologically independent samples. (f-g) Representative ratiometric images (f) and quantification (g) of crowding sensor FRET expressed in the same HEK293T cell before and after 0.2M sorbitol treatment. Rainbow RGB look-up table showing changes in FRET indices. Color bar: FRET index (a.u.). Two-sided paired t-test. Center of the data is mean. Error bars show SEM. Scale bars are 5μm. n=31 biologically independent samples. Statistics source data are provided in Source Data Extended Data Figure 2.

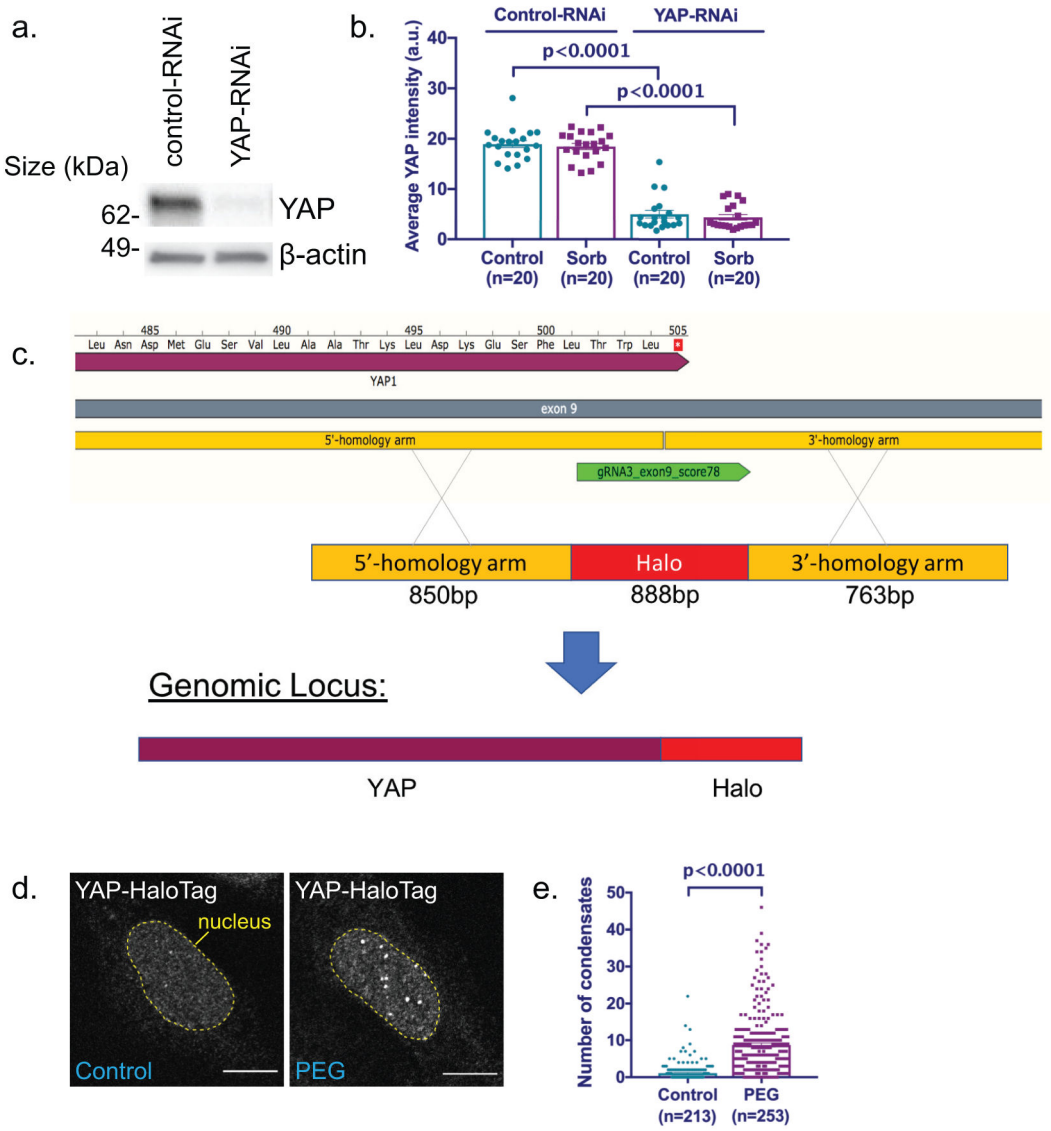

Extended Data Fig. 3. Endogenous YAP forms condensates.

(a-b) Immunoblotting experiments (a) and quantifications of immunofluorescence YAP signal (b) indicate that YAP signal is effectively knocked down by YAP siRNA. Two-sided unpaired t-test is used in b. Center of the data is mean. Error bars show SEM. All the experiments are repeated 2 times independently with similar results. n=20 biologically independent samples. (c) Schematics of construction of CRISPR knock-in YAP-HaloTag U-2 OS cell line. Live-cell imaging (d) and quantification (e) showing nuclear YAP-HaloTag condensate labelled by JF549 Halo dye increases in number after PEG 300 treatment. Two-sided unpaired t-test analysis. Center of the data is mean. Error bars show SEM. Scale bars are 10μm. n=213 biologically independent control samples. n=253 biologically independent PEG-treated samples. Statistics source data are provided in Source Data Extended Data Figure 3. Unprocessed blots are provided in Unprocessed Blots Extended Data Figure 3.

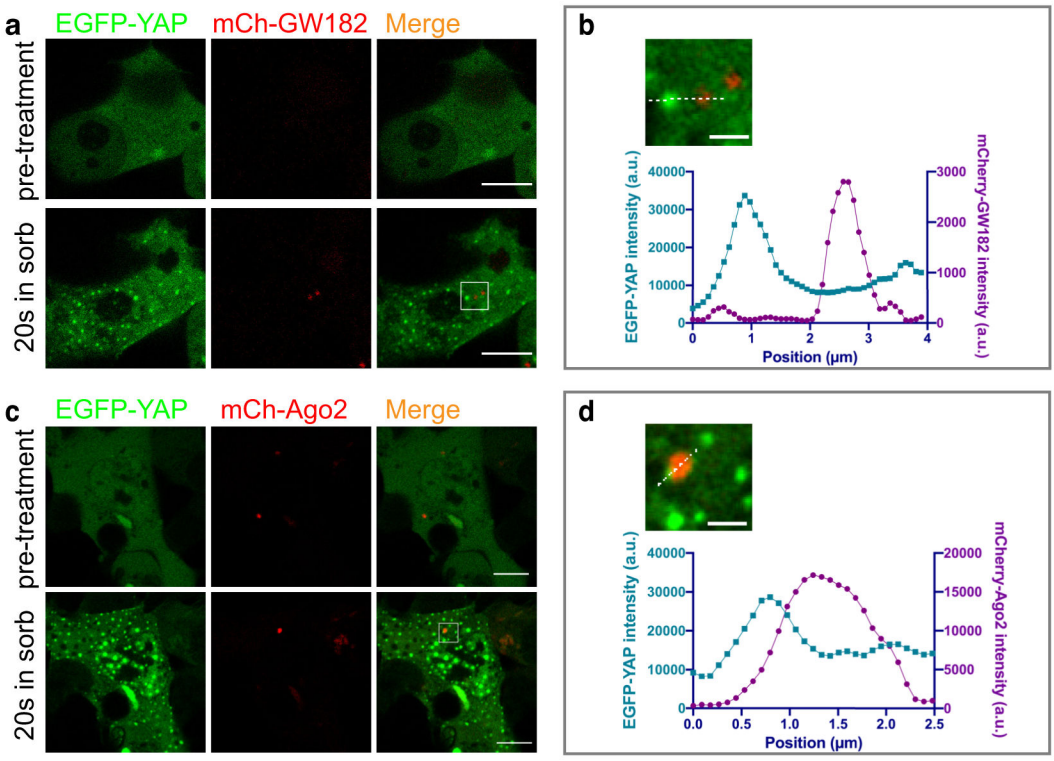

Extended Data Fig. 4. Characterization of cytoplasmic YAP condensates.

(a) Live-cell imaging showing no colocalization of cytoplasmic EGFP-YAP condensates with P-body component mCherry-GW182 after 0.2M sorbitol treatment for 20 sec in HEK293T cells. (b) Magnification of boxed region in (a) and line-scan. (c-d) Similar to (a-b), showing no colocalization of EGFP-YAP cytoplasmic condensates with mCherry-Ago2 after 0.2M sorbitol treatment for 20 sec. Scale bars are 10μm in whole cell view, and are 2μm in magnified view. All the experiments are repeated 3 times independently with similar results. Numerical source data are provided in Source Data Extended Data Figure 4.

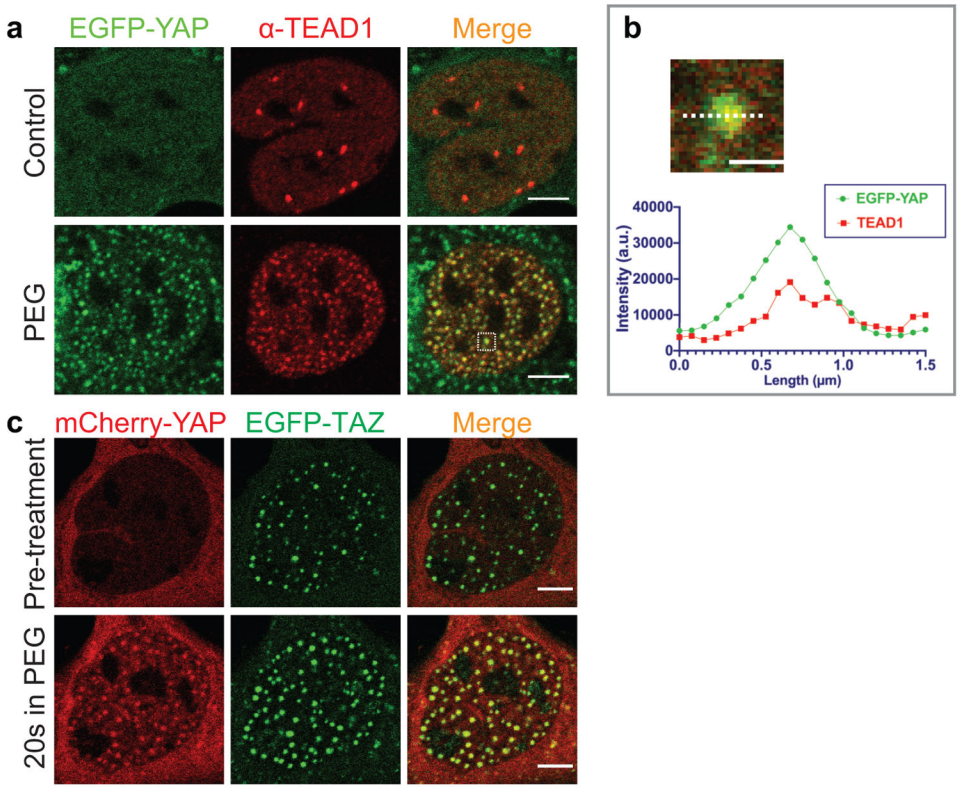

Extended Data Fig. 5. Characterization of nuclear YAP condensates.

(a) Representative immunofluorescence images showing EGFP-YAP nuclear condensates colocalize with endogenous TEAD1 under hyperosmotic stress in U-2 OS cells. (b) Magnification of boxed region in a, and line scan. Scale bar: 1μm. (c) Live-cell imaging showing mCherry-YAP localizes to EGFP-TAZ condensates and new condensates after hyperosmotic stress in U-2 OS cells. Scale bars in (a) and (c) are 5μm. All the experiments are repeated 3 times independently with similar results. Numerical source data are provided in Source Data Extended Data Figure 5.

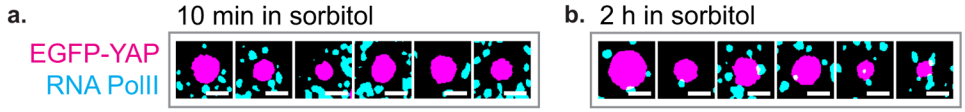

Extended Data Fig. 6. Dynamic localization of RNAPII relative to EGFP-YAP nuclear condensates after hyperosmotic shock.

(a) More examples showing no colocalization of RNAPII (pSer2) with EGFP-YAP condensates at 10min in 0.2M sorbitol. Experiments are same as those in Fig. 7b, EGFP-YAP condensates are auto-thresholded and turned into mask using ImageJ, and pseudo-colored magenta. RNAPII immunofluorescence is autothresholded and turned into mask using ImageJ, and pseudo-colored cyan. (b) Similar to a, but showing more examples of enhanced localization of RNA Pol ll (pSer2) to the periphery of EGFP-YAP condensates at 2 h in sorbitol. All the experiments are repeated 3 times independently with similar results. Scale bars are 1μm.

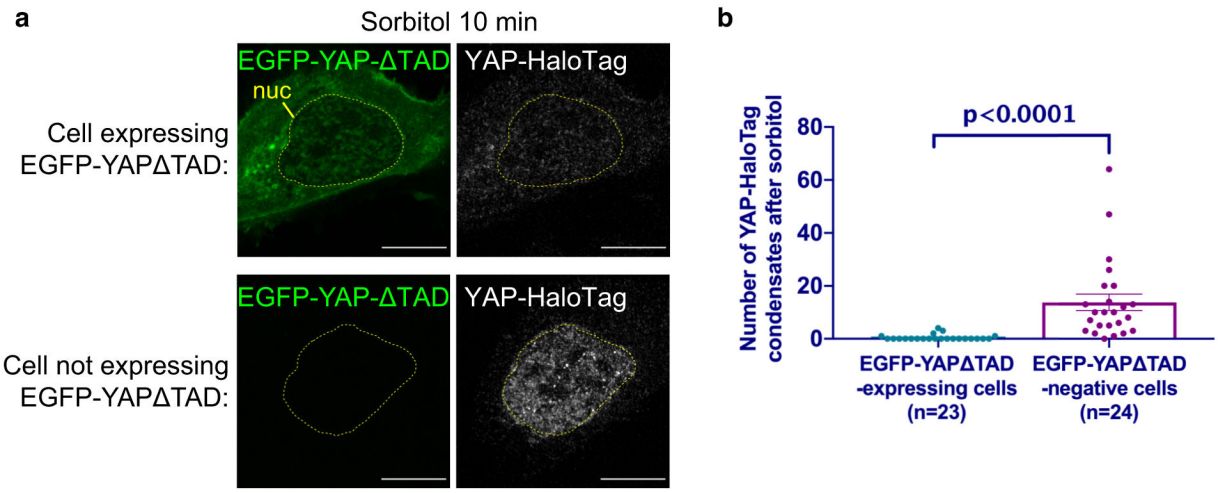

Extended Data Fig. 7. EGFP-YAPΔTAD mutant serves as a dominant negative protein that decreases endogenous YAP foci.

(a) Immunofluorescence images of YAP-HaloTag U-2 OS cells 10 min in sorbitol treatment, with EGFP-YAPΔTAD overexpression (top row) or without (bottom row). Scale bars are 10μm. (b) Quantification showing YAP-HaloTag U-2 OS cells have lower number of YAP-HaloTag endogenous YAP condensates after sorbitol treatment for 10 min, if they overexpress EGFP-YAPΔTAD construct. Two-sided unpaired t-test. Center of the data is mean. Error bars show SEM. n=23 biologically independent EGFP-YAPΔTAD-expressing samples. n=24 biologically independent EGFP-YAPΔTAD-negative samples. Statistics source data are provided in Source Data Extended Data Figure 8.

Supplementary Material

Refer to Web version on PubMed Central for supplementary material.

Acknowledgements

We thank members of the Jennifer Lippincott-Schwartz lab for helpful discussions and critical comments. Support for this work was from Howard Hughes Medical Institute (Jennifer Lippincott-Schwartz and Zhe Liu), Damon Runyon Cancer Research Foundation (DRG-2233-15, Danfeng Cai), and intramural research funding from NIH. We also appreciate the help from Flow Cytometry Core Facility of NEI/NIH.

Reference:

1. Pan D The hippo signaling pathway in development and cancer. Dev Cell 19, 491–505, doi:10.1016/j.devcel.2010.09.011 (2010). [PubMed: 20951342]
2. Zanconato F, Cordenonsi M & Piccolo S YAP/TAZ at the Roots of Cancer. Cancer Cell 29, 783–803, doi:10.1016/j.ccell.2016.05.005 (2016). [PubMed: 27300434]
3. Lian I et al. The role of YAP transcription coactivator in regulating stem cell self-renewal and differentiation. Gene Dev 24, 1106–1118, doi:10.1101/gad.1903310 (2010). [PubMed: 20516196]
4. Dupont S et al. Role of YAP/TAZ in mechanotransduction. Nature 474, 179–183, doi:10.1038/nature10137 (2011). [PubMed: 21654799]
5. Deran M et al. Energy Stress Regulates Hippo-YAP Signaling Involving AMPK-Mediated Regulation of Angiomotin-like 1 Protein. Cell Rep 9, 495–503, doi:10.1016/j.celrep.2014.09.036 (2014). [PubMed: 25373897]

6. Hong AW et al. Osmotic stress-induced phosphorylation by NLK at Ser128 activates YAP. EMBO Rep 18, 72–86, doi:10.15252/embr.201642681 (2017). [PubMed: 27979971]
7. Shin Y & Brangwynne CP Liquid phase condensation in cell physiology and disease. Science 357, doi:10.1126/science.aaf4382 (2017).
8. Banani SF, Lee HO, Hyman AA & Rosen MK Biomolecular condensates: organizers of cellular biochemistry. Nat Rev Mol Cell Biol 18, 285–298, doi:10.1038/nrm.2017.7 (2017). [PubMed: 28225081]
9. Jain A & Vale RD RNA phase transitions in repeat expansion disorders. Nature 546, 243–+, doi:10.1038/nature22386 (2017). [PubMed: 28562589]
10. Strom AR et al. Phase separation drives heterochromatin domain formation. Nature 547, 241–245, doi:10.1038/nature22989 (2017). [PubMed: 28636597]
11. Larson AG et al. Liquid droplet formation by HP1 alpha suggests a role for phase separation in heterochromatin. Nature 547, 236–+, doi:10.1038/nature22822 (2017). [PubMed: 28636604]
12. Sabari BR et al. Coactivator condensation at super-enhancers links phase separation and gene control. Science, doi:10.1126/science.aar3958 (2018).
13. Boija A et al. Transcription Factors Activate Genes through the Phase-Separation Capacity of Their Activation Domains. Cell 175, 1842–+, doi:10.1016/j.cell.2018.10.042 (2018). [PubMed: 30449618]
14. Cho WK et al. Mediator and RNA polymerase II clusters associate in transcription-dependent condensates. Science, doi:10.1126/science.aar4199 (2018).
15. Hnisz D, Shrinivas K, Young RA, Chakraborty AK & Sharp PA A Phase Separation Model for Transcriptional Control. Cell 169, 13–23, doi:10.1016/j.cell.2017.02.007 (2017). [PubMed: 28340338]
16. Hnisz D et al. Super-enhancers in the control of cell identity and disease. Cell 155, 934–947, doi:10.1016/j.cell.2013.09.053 (2013). [PubMed: 24119843]
17. Galli GG et al. YAP Drives Growth by Controlling Transcriptional Pause Release from Dynamic Enhancers. Mol Cell 60, 328–337, doi:10.1016/j.molcel.2015.09.001 (2015). [PubMed: 26439301]
18. Zanconato F et al. Transcriptional addiction in cancer cells is mediated by YAP/TAZ through BRD4. Nat Med 24, 1599–+, doi:10.1038/s41591-018-0158-8 (2018). [PubMed: 30224758]
19. Lin Y, Protter DSW, Rosen MK & Parker R Formation and Maturation of Phase-Separated Liquid Droplets by RNA-Binding Proteins. Mol Cell 60, 208–219, doi:10.1016/j.molcel.2015.08.018 (2015). [PubMed: 26412307]
20. Smith J et al. Spatial patterning of P granules by RNA-induced phase separation of the intrinsically-disordered protein MEG-3. Elife 5, doi:10.7554/eLife.21337 (2016).
21. Alberti S, Gladfelter A & Mittag T Considerations and Challenges in Studying Liquid-Liquid Phase Separation and Biomolecular Condensates. Cell 176, 419–434, doi:10.1016/j.cell.2018.12.035 (2019). [PubMed: 30682370]
22. Gottschalk CW & Mylle M Micropuncture study of the mammalian urinary concentrating mechanism: evidence for the countercurrent hypothesis. Am J Physiol 196, 927–936, doi:10.1152/ajplegacy.1959.196.4.927 (1959). [PubMed: 13637248]
23. Wirz H Kidney, water and electrolyte metabolism. Annu Rev Physiol 23, 577–606, doi:10.1146/annurev.ph.23.030161.003045 (1961). [PubMed: 13785983]
24. Guyton A & Hall J Regulation of extracellular fluid osmolarity and sodium concentration. Textbook of medical physiology, 349–365 (2006).
25. Jamison RL & Maffly RH The urinary concentrating mechanism. New England Journal of Medicine 295, 1059–1067 (1976).
26. Dong JX et al. Elucidation of a universal size-control mechanism in Drosophila and mammals. Cell 130, 1120–1133, doi:10.1016/j.cell.2007.07.019 (2007). [PubMed: 17889654]
27. Hao YW, Chun A, Cheung K, Rashidi B & Yang XL Tumor suppressor LATS1 is a negative regulator of oncogene YAP. J Biol Chem 283, 5496–5509, doi:DOI 10.1074/jbc.M709037200 (2008). [PubMed: 18158288]
28. Moon S et al. Phosphorylation by NLK inhibits YAP-14-3-3-interactions and induces its nuclear localization. EMBO Rep 18, 61–71, doi:10.15252/embr.201642683 (2017). [PubMed: 27979972]

29. Vassilev A, Kaneko KJ, Shu H, Zhao Y & DePamphilis ML TEAD/TEF transcription factors utilize the activation domain of YAP65, a Src/Yes-associated protein localized in the cytoplasm. Genes Dev 15, 1229–1241, doi:10.1101/gad.888601 (2001). [PubMed: 11358867]
30. Zhao B et al. TEAD mediates YAP-dependent gene induction and growth control. Genes Dev 22, 1962–1971, doi:10.1101/gad.1664408 (2008). [PubMed: 18579750]
31. Wu T et al. Phase separation of TAZ compartmentalizes the transcription machinery to promote gene expression. bioRxiv, 671230, doi:10.1101/671230 (2019).
32. Boyle AP et al. High-resolution mapping and characterization of open chromatin across the genome. Cell 132, 311–322, doi:10.1016/j.cell.2007.12.014 (2008). [PubMed: 18243105]
33. Wu C The 5′ ends of Drosophila heat shock genes in chromatin are hypersensitive to DNase I. Nature 286, 854–860, doi:10.1038/286854a0 (1980). [PubMed: 6774262]
34. Buenrostro JD, Giresi PG, Zaba LC, Chang HY & Greenleaf WJ Transposition of native chromatin for fast and sensitive epigenomic profiling of open chromatin, DNA-binding proteins and nucleosome position. Nat Methods 10, 1213–+, doi:10.1038/Nmeth.2688 (2013). [PubMed: 24097267]
35. Xie L et al. Super-resolution Imaging Reveals 3D Structure and Organizing Mechanism of Accessible Chromatin. bioRxiv, 678649, doi:10.1101/678649 (2019).
36. Betzig E et al. Imaging intracellular fluorescent proteins at nanometer resolution. Science 313, 1642–1645, doi:10.1126/science.1127344 (2006). [PubMed: 16902090]
37. Chen BC et al. Lattice light-sheet microscopy: Imaging molecules to embryos at high spatiotemporal resolution. Science 346, 439–+, doi:UNSP 1257998 10.1126/science.1257998 (2014).
38. Legant WR et al. High-density three-dimensional localization microscopy across large volumes. Nat Methods 13, 359–365, doi:10.1038/Nmeth.3797 (2016). [PubMed: 26950745]
39. Zhao B, Li L, Tumaneng K, Wang CY & Guan KL A coordinated phosphorylation by Lats and CK1 regulates YAP stability through SCF beta-TRCP. Gene Dev 24, 72–85, doi:10.1101/gad.1843810 (2010). [PubMed: 20048001]
40. Shin Y et al. Spatiotemporal Control of Intracellular Phase Transitions Using Light-Activated optoDroplets. Cell 168, 159–+, doi:10.1016/j.cell.2016.11.054 (2017). [PubMed: 28041848]
41. Shin Y et al. Liquid Nuclear Condensates Mechanically Sense and Restructure the Genome. Cell 176, 1518, doi:10.1016/j.cell.2019.02.025 (2019). [PubMed: 30849377]
42. Bracha D et al. Mapping Local and Global Liquid Phase Behavior in Living Cells Using Photo-Oligomerizable Seeds (vol 175, 1467.e1, 2018). Cell 176, 407–407, doi:10.1016/j.cell.2018.12.026 (2019). [PubMed: 30633909]
43. Ran FA et al. Genome engineering using the CRISPR-Cas9 system. Nat Protoc 8, 2281–2308, doi:10.1038/nprot.2013.143 (2013). [PubMed: 24157548]
44. Chen XQ et al. ATAC-see reveals the accessible genome by transposase-mediated imaging and sequencing. Nature methods 13, 1013–+, doi:10.1038/Nmeth.4031 (2016). [PubMed: 27749837]

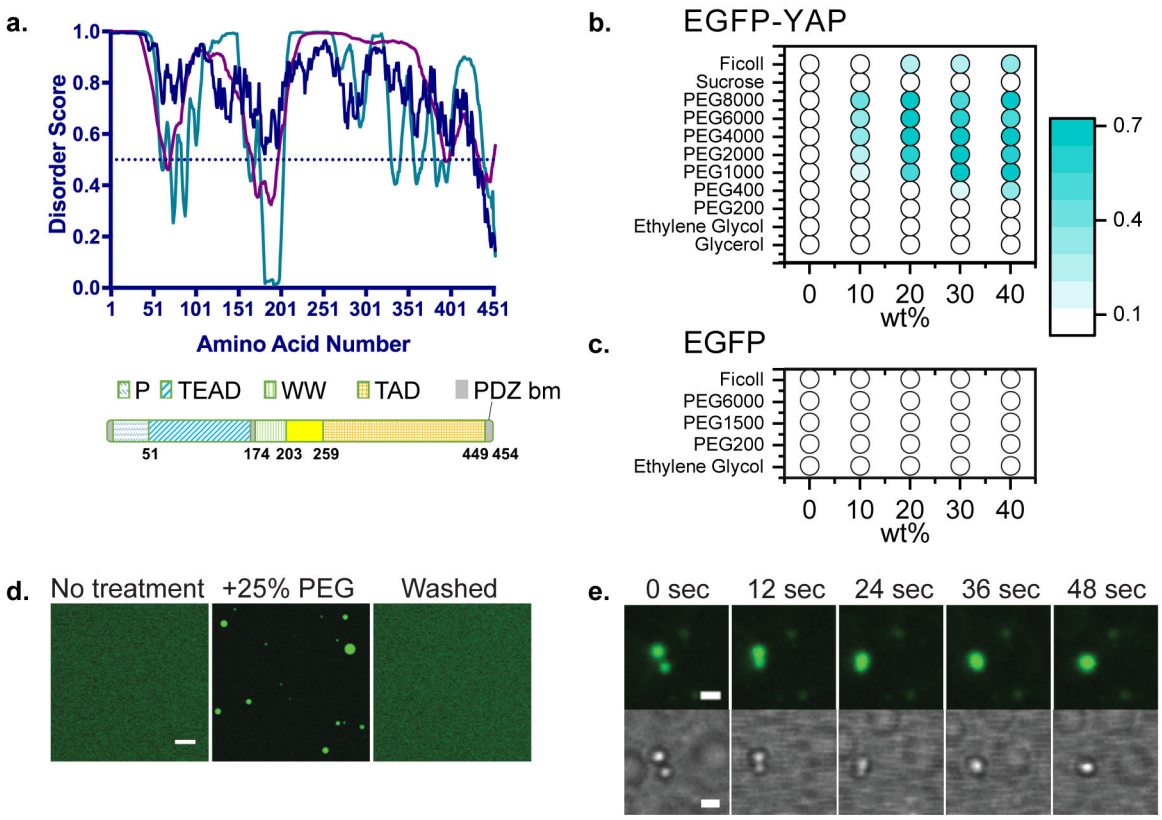

Fig. 1. YAP has intrinsic property to phase separate.

(a) Disorder analysis of YAP 454aa isoform. Algorithms used: IUPred (blue), VLXT (cyan) and VSL2 (magenta). (b-c) Purified EGFP-YAP shows concentration-dependent increase in turbidity at increasing wt% of large polymeric crowders (b) while purified EGFP does not (c). Color bar: turbidity measured at 600nm (a.u.). (d) EGFP-YAP pre-treatment (left) and after the addition of 25% PEG (middle). Upon centrifugation and resuspension in isotonic buffer, the droplets disappear (right). Scale bar, 10μm. The experiment has been repeated 3 times independently with similar results. (e) Droplet coalescence shown in fluorescence (top) and brightfield (bottom) illumination. Scale bars: 2μm. The experiment has been repeated 3 times independently with similar results.

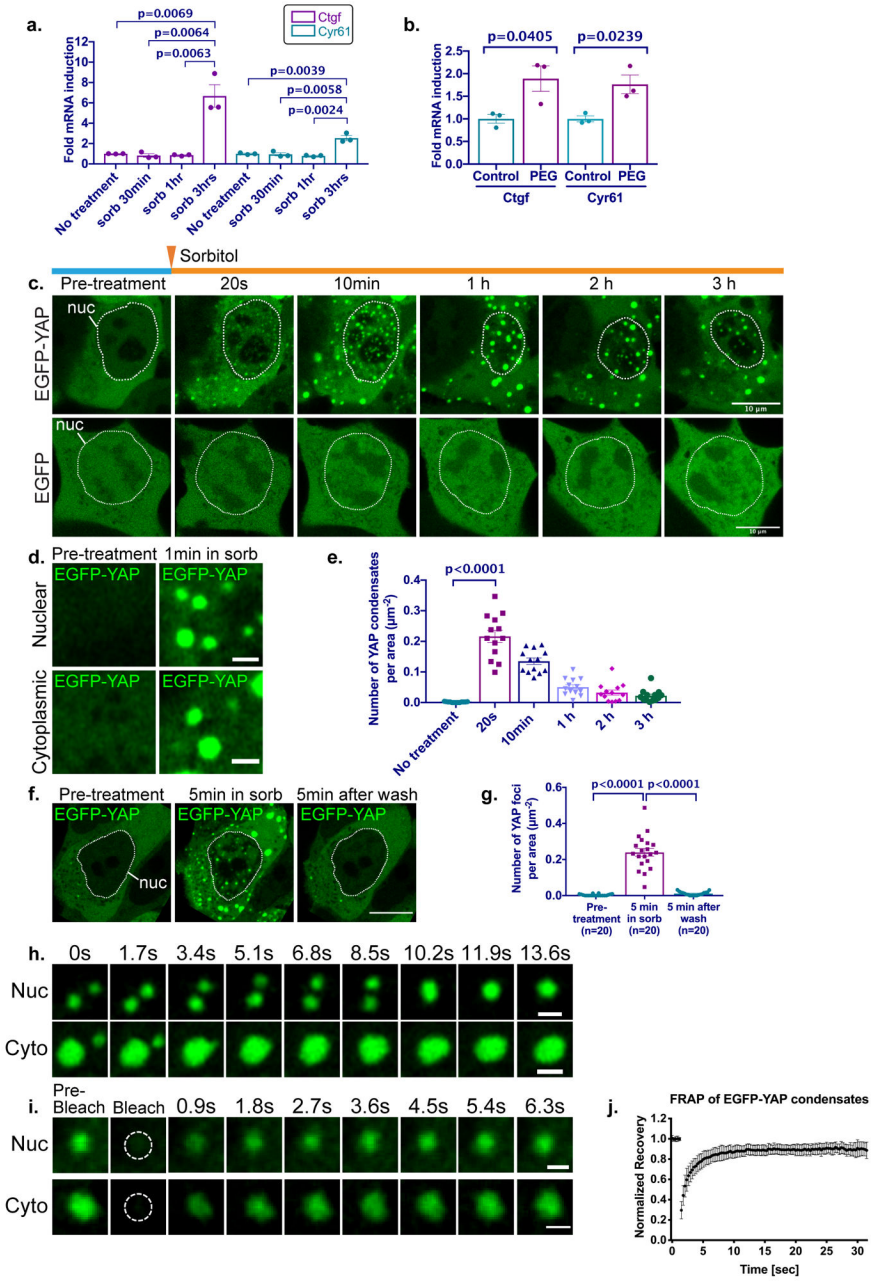

Fig. 2. YAP undergoes phase separation under hyperosmotic stress.

(a) Quantification of relative Ctgf and Cyr61 mRNAs levels in control and sorbitol-treated HEK293T cells expressing EGFP-YAP. Two-sided unpaired t-test. Center of the data is mean. Error bars are SEM. n=3 biologically independent samples. (b) Quantification of relative Ctgf and Cyr61 mRNAs levels in control and 5% PEG 300-treated HEK293T cells expressing EGFP-YAP. 3hrs after indicated treatments. Two-sided unpaired t-test. Center of the data is mean. Error bars are SEM. n=3 biologically independent samples. (c) EGFP-YAP localizes to the nucleus of HEK293T cells and forms cytoplasmic and nuclear foci 20 sec after sorbitol treatment, while EGFP doesn't. Scale bars: 10μm. (d) Zoomed-up live-cell imaging of nuclear and cytoplasmic YAP condensates formed after 1 min in sorbitol. Scale

bars: 1μm. (e) Quantification of number of EGFP-YAP foci in the HEK293T cell at indicated time after sorbitol treatment normalized by cell area. Two-sided paired t-test. Center of the data is mean. Error bars are SEM. n=13 biologically independent samples. (f) Live-cell imaging showing EGFP-YAP condensate formation is reversible. Scale bar: 10μm. (g) Quantification of reversible EGFP-YAP condensate formation. Two-sided paired t-test. Center of the data is mean. Error bars are SEM. (h) Time-lapse imaging of fusion of nuclear and cytoplasmic EGFP-YAP droplets. The experiment has been repeated at least 5 times independently with similar results. (i) FRAP recovery images and quantification of nuclear or cytoplasmic EGFP-YAP condensates. Dotted circle: Spot of photobleaching. Scale bars in (h) and (i) are 1μm. (j) FRAP recovery curve of EGFP-YAP condensates, averaged over 26 experiments. Error bars show SD. Dotted lines indicate the location of the nucleus of HEK293T cells. Center of the data is mean. n= 26 biologically independent experiments. Statistics source data are provided in Source Data Figure 2.

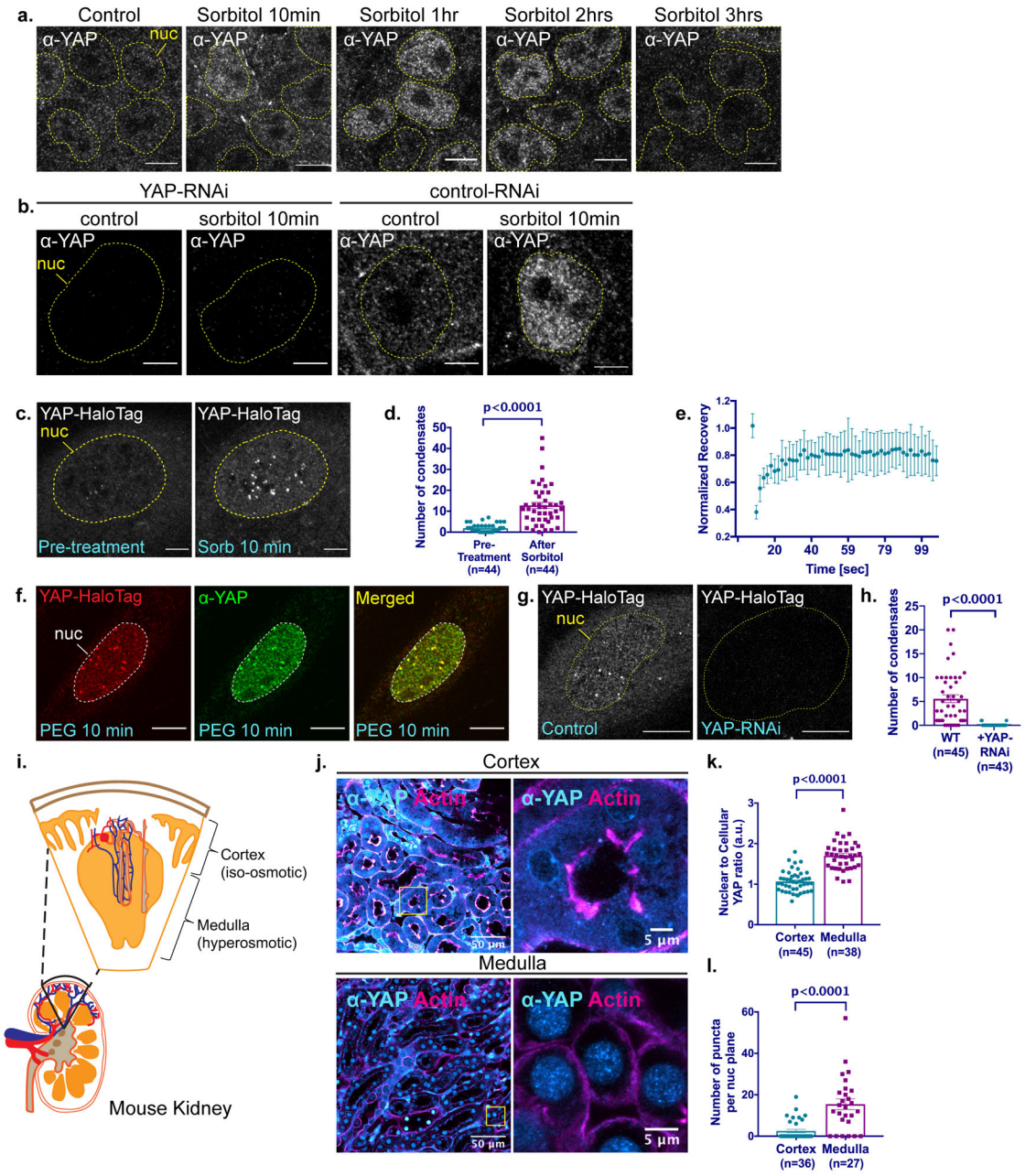

Fig. 3. Endogenous YAP form condensates.

(a) Endogenous YAP in HEK293T cells visualized by immunofluorescence using antibody staining, showing rapid localization of endogenous YAP to the nucleus. The experiment is repeated 4 times independently with similar results. Scale bars are 10μm. (b) Immunofluorescence images showing endogenous YAP in HEK293T cells form condensates in response to 0.2M sorbitol treatment for 10 min. YAP signal in both diffuse and condensate form is depleted by RNAi against YAP. The experiment is repeated 3 times independently with similar results. Scale bars are 5μm. (c-h) Endogenous Halo-tagged YAP form condensates in U-2 OS cells, visualized by Airyscan live-cell imaging. Live-cell imaging (c) and quantification (d) showing nuclear Halo-YAP condensate labelled by JF549

Halo dye increases in number after sorbitol treatment. Two-sided paired t-test. Center of the data is mean. Error bars show SEM. n=44 biologically independent samples (e) FRAP recovery curve of YAP-HaloTag condensate in sorbitol-treated cells. Center of the data is mean. Error bars are SD. n=12 biologically independent experiments. (f) Immunofluorescence showing YAP-HaloTag (labelled with JF549 Halo dye) colocalizes with endogenous YAP labeled with YAP antibody in cells treated with 10% PEG300 for 10 min. Experiment has been repeated 3 times independently with similar results. (g-h) Live-cell imaging by Airyscan (g) and quantifications (h) showing YAP RNAi knocks down YAP-HaloTag signal in both diffuse and condensate form. Error bars show SEM. Two-sided unpaired t-test. Center of the data is mean. n=45 biologically independent control samples. n=43 biologically independent YAP-RNAi samples. Scale bars in c are 5μm, in f-g are 10μm.

(i-l) Medulla region cells in the mouse kidney have nuclear YAP in condensate form. (i) Illustration of a kidney and relative locations of cortex and medulla. (j) Representative YAP immunofluorescence images of mouse kidney cells at cortex and medulla regions. Larger field of view shown on left (Scale bars: 50μm), and the yellow boxed regions are magnified and shown on right (Scdale bars: 5μm). (k) Quantification of nuclear to cellular ratio of YAP in indicated regions. Two-sided unpaired t-test. Center of the data is mean. Error bars are SEM. n=45 biologically independent cortical cell samples. n=38 biologically independent medulla cell samples. (l) Quantification of number of condensates in nuclei of kidney cells with visible condensates. Two-sided unpaired t-test. Center of the data is mean. Error bars are SEM. n=36 biologically independent cortical cell samples. n=27 biologically independent medulla cell samples. Statistics source data are provided in Source Data Figure 3.

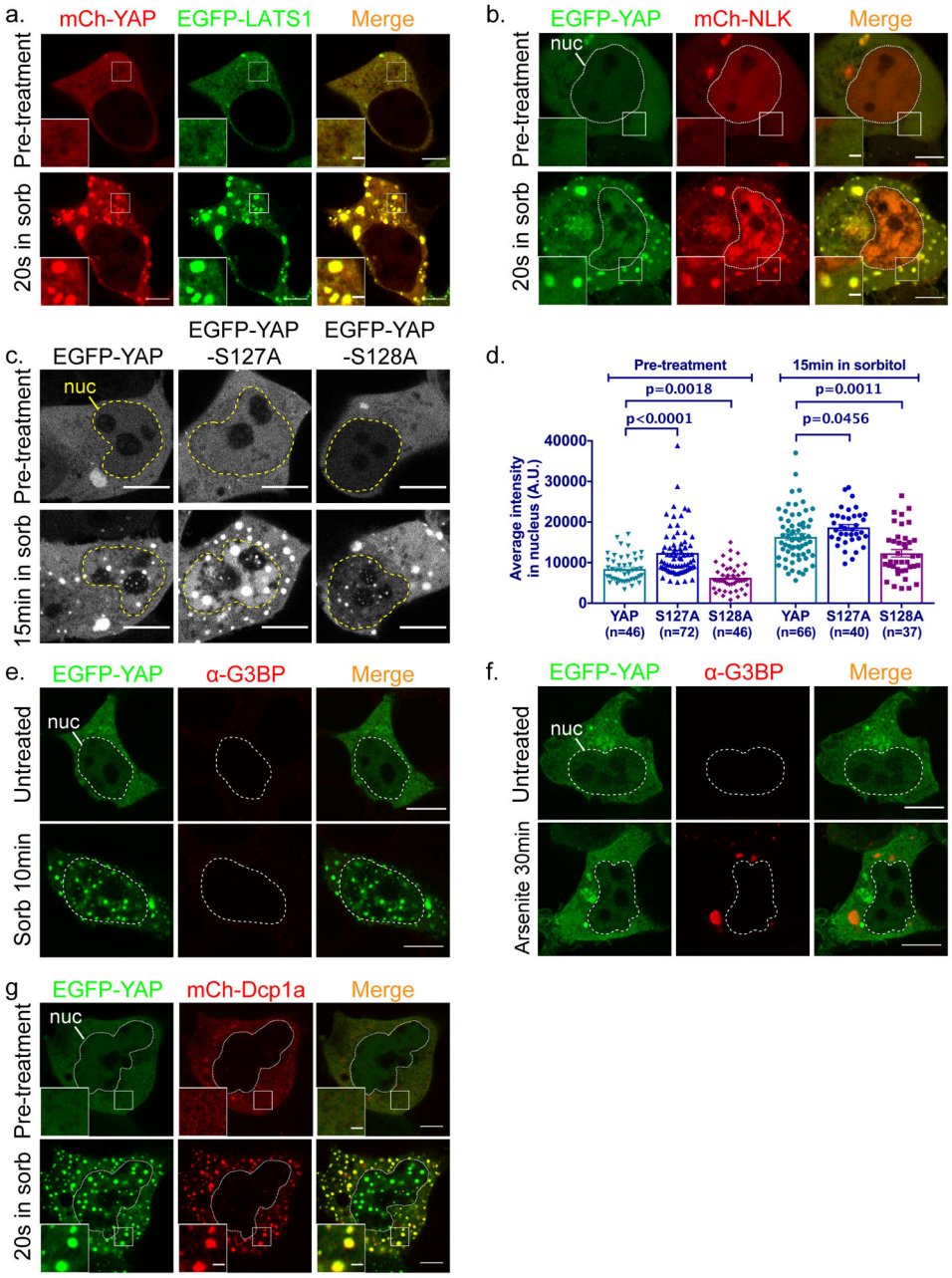

Fig. 4. Cytoplasmic EGFP-YAP selectively enrich different proteins.

(a) Live-cell imaging showing colocalization of mCherry-YAP condensates with EGFP-LATS1 condensates in the cytoplasm of HEK293T cells after hyperosmotic stress. The experiment is repeated 3 times independently with similar results. (b) Live-cell imaging showing colocalization of EGFP-YAP condensates with mCherry-NLK condensates in the cytoplasm of HEK293T cells after hyperosmotic stress. The experiment is repeated 3 times independently with similar results. (c) Live-cell imaging of HEK293T cells showing EGFP-YAP wildtype and mutants are able to form condensates with sorbitol treatment, although nuclear localization before and after sorbitol treatment changes, quantified in (d). Comparisons are done between mutants and WT YAP, using two-sided unpaired t-test.

Center of the data is mean. In samples pre-treatment, n=46 biologically independent samples for calculating YAP intensity in the nucleus, n=72 biologically independent samples for calculating S127A intensity in the nucleus, and n=46 biologically independent samples for calculating S128A intensity in the nucleus. In sorbitol-treated samples, n=66 biologically independent samples for calculating YAP intensity in the nucleus, n=40 biologically independent samples for calculating S127A intensity in the nucleus,and n=37 biologically independent samples for calculating S128A intensity in the nucleus. (e) Representative immunofluorescence images showing 0.2M sorbitol treatment for 20 sec induces EGFP-YAP condensate formation in HEK293T cells but not stress granule formation (visualized by G3BP antibody). The experiment is repeated 3 times independently with similar results. (f) Representative immunofluorescence images showing 0.5mM arsenite treatment for 30 min induces stress granule formation but not YAP condensate formation. The experiment is repeated 3 times independently with similar results. (g) Live-cell imaging showing colocalization of EGFP-YAP condensates with mCherry-Dcp1a condensates in the cytoplasm of HEK293T cells after hyperosmotic stress. The experiment is repeated 3 times independently with similar results. In a, b, g: scale bars are 5μm in whole-cell images, and 1μm in magnified views of boxed regions. In c, e, and f: scale bars are 10μm. Statistics source data are provided in Source Data Figure 4.

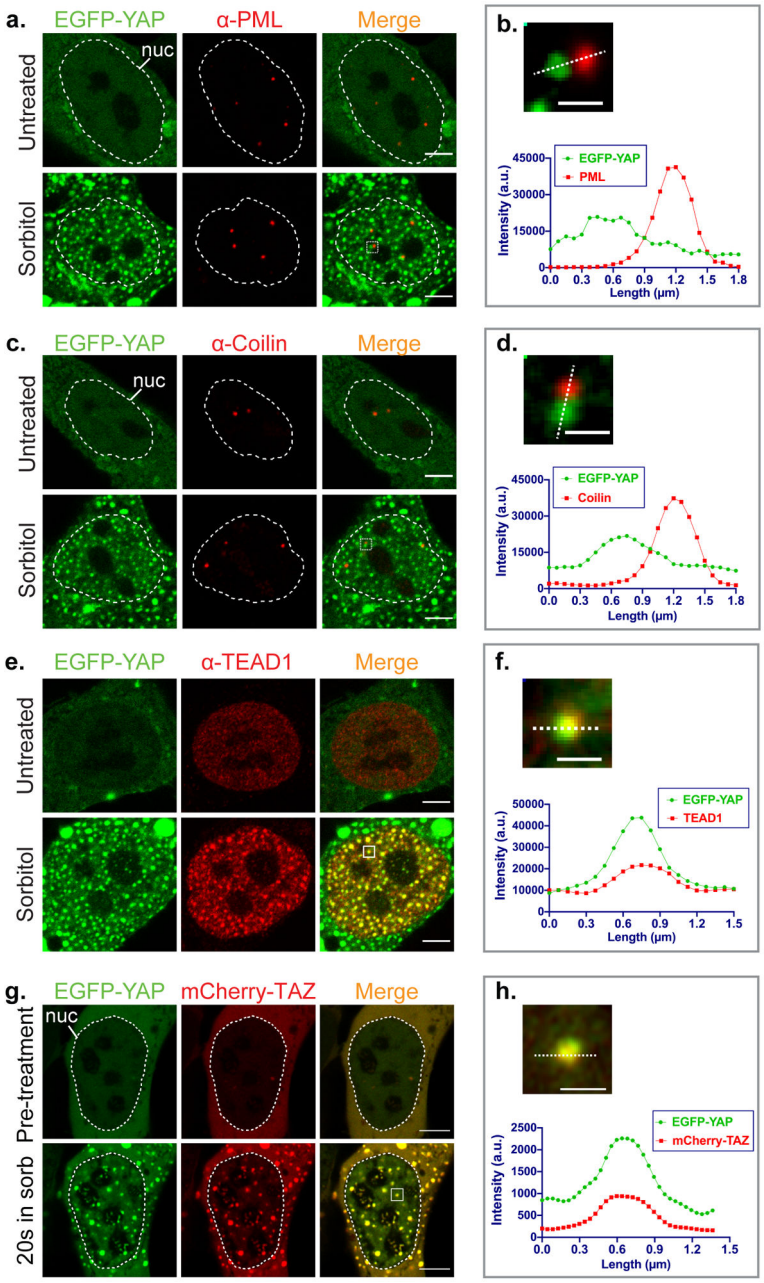

Fig. 5. Nuclear EGFP-YAP selectively enrich transcription-related proteins.

(a) Immunofluorescence showing no colocalization of PML staining with EGFP-YAP before or after hyperosmotic shock. (b) Magnification of inset of bottom right image of (a) and line-scan. (c-d) Cajal bodies (visualized by anti-Coilin immunofluorescence) don't colocalize with EGFP-YAP before or after hyperosmotic shock in HEK293T cells. Similar to (a-b). (e) Immunofluorescence showing TEAD1 colocalizes with nuclear EGFP-YAP condensates under hyperosmotic stress. (f) Magnification of the boxed region in (g), and line plot of the dotted line. (g) Live-cell imaging showing colocalization of mCherry-TAZ with EGFP-YAP 20 sec after hyperosmotic stress. (h) Magnification of the boxed region in (j), and line plot of the dotted line. Scale bars are 5μm in a, c, e, g and 1μm in b, d, f, j. All the experiments are

repeated 3 times independently with similar results. Statistics source data are provided in Source Data Figure 5.

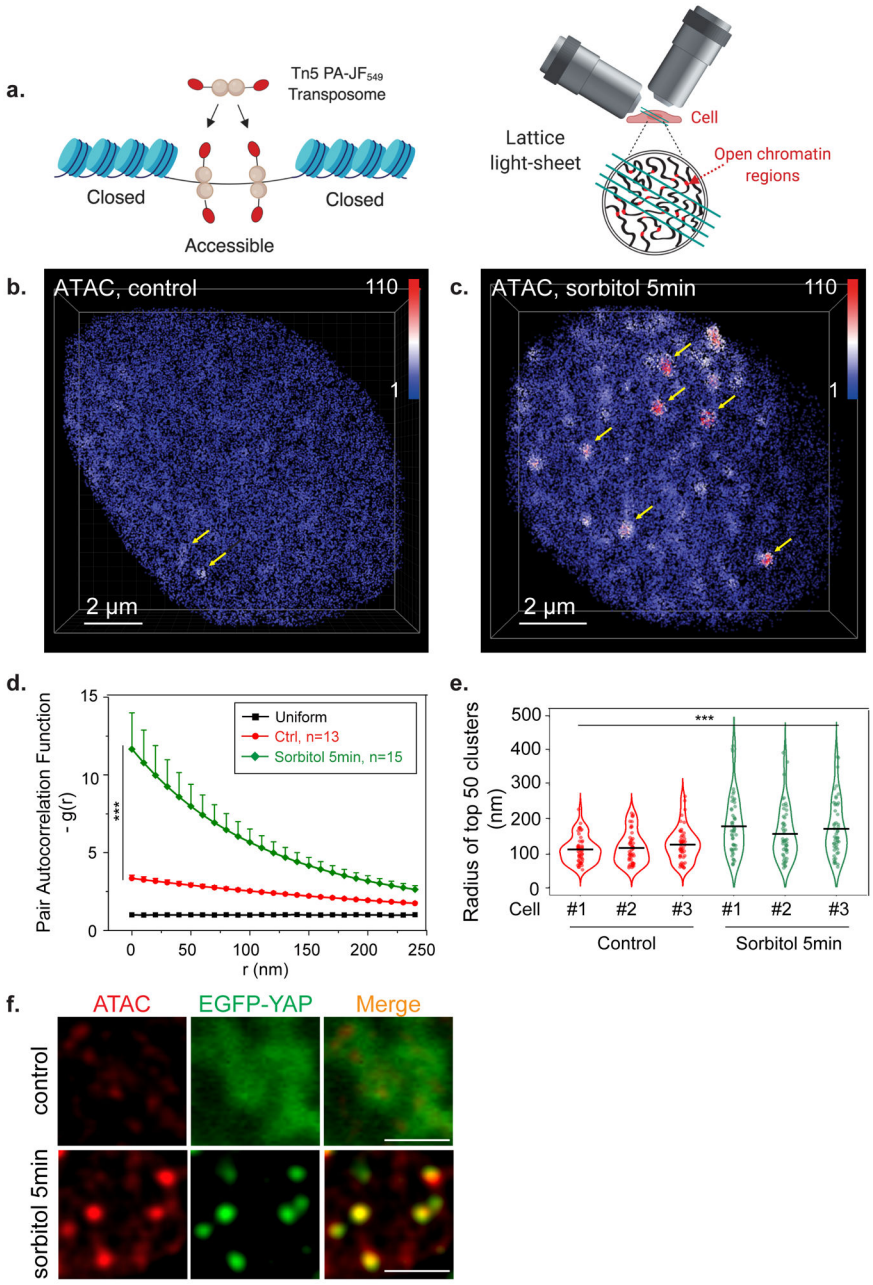

Fig. 6. YAP condensates induced by sorbitol treatment alter 3D organization of accessible chromatin.

(a) Schematics of the 3D ATAC-PALM microscopy labeling and imaging strategy. Photoactivatable Janelia Fluor 549 (PA-JF549) was conjugated to DNA oligo containing the mosaic ends (ME) of the Tn5 transposon and reconstituted with Tn5 transposase (cyan) to form the active transposome complex in vitro (left panel). The cells were then fixed, permeabilized, and accessible sites in the genome were selectively labeled by the reconstituted active transposome complex before mounting onto the Lattice Light Sheet microscope for 3D ATAC-PALM imaging. (b-c) 3D image of accessible chromatin localizations in control (b) and 5min sorbitol-treated (c) HEK293T cells. The color-coded

localization density was calculated with a canopy radius of 250nm. Yellow arrows point to ATAC clusters identified. Scale bars are 2μm. (d) Global pair auto-correlation function g(r) analysis of ATAC-PALM localizations for control and sorbitol-treated HEK 293 cells. The error bars represent SEM. The non-parametric two-sided Mann-Whitney U test was used to compare the clustering amplitude A (equals to g(0)) in different groups. g(r) was plotted from the fitted exponential decay function. Center of the data is mean. $p= 1.49\times10^{-5}$. n=13 biologically independent control-treated cells. n=15 biologically independent sorbitol-treated cells. (e) Violin plot shows the normalized radii of top 50 identified accessible chromatin clusters in control and sorbitol-treated HEK293T cells identified by DBSCAN algorithm. The radius of each cluster was plotted as a dot and the violin plot shows the distribution of these 50 data points. n=10 biologically independent samples. For statistical analysis, data from three individual cells for each condition were pooled together and two-sided Mann-Whitney U test was applied. Bars indicate the median values of each group. $p= 2\times10^{-8}$. (f) Example images show colocalization of identified accessible chromatin clusters and YAP condensates in control and sorbitol-treated HEK293T cells. To derive the ATAC-PALM intensity map (red) in order to compare with EGFP-YAP signal, ATAC-PALM localizations were binned within a cubic of 100 nm with a 3D Gaussian filter and a convolution kernel of 3×3×3. Scale bar: 2 μm. Experiments were repeated 3 times independently and showed similar results. Statistics source data are provided in Source Data Figure 6.

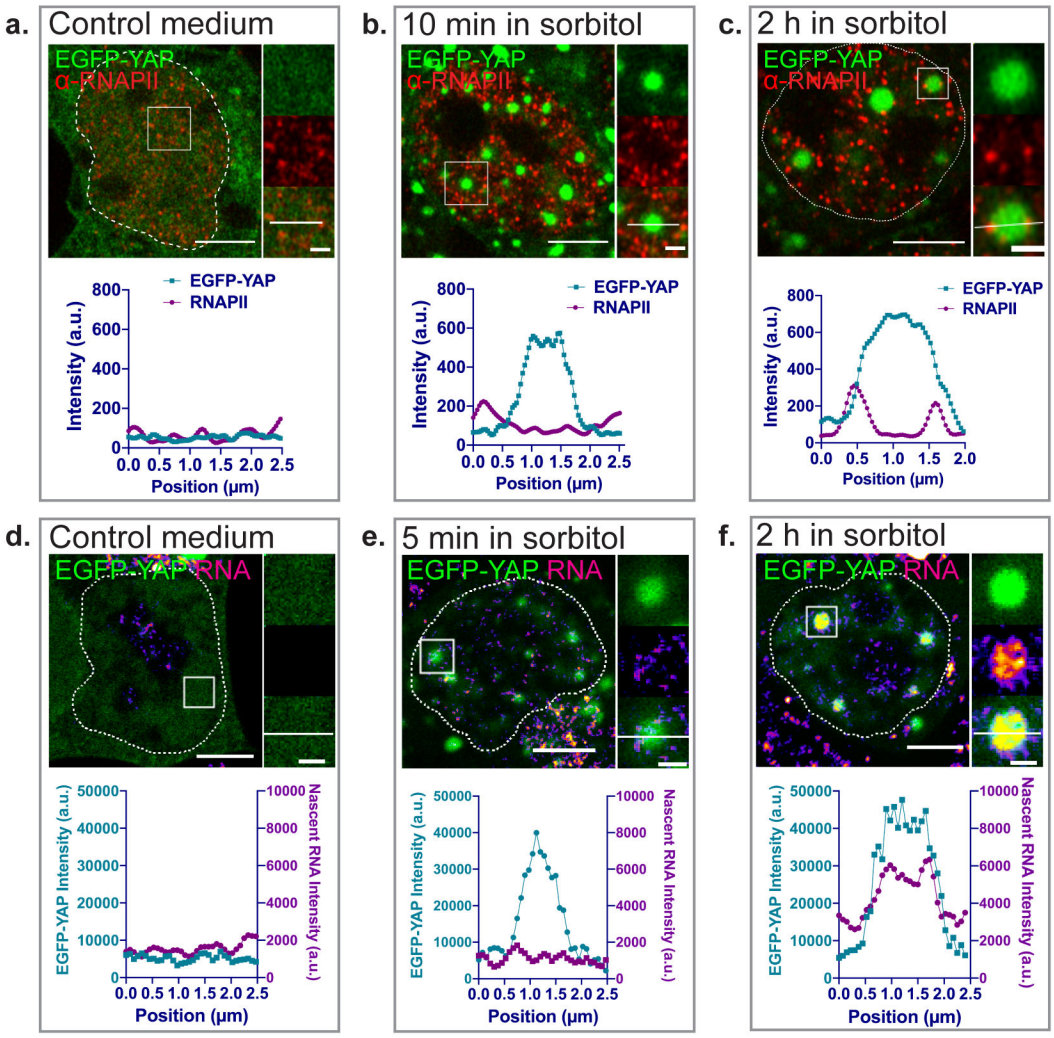

Fig. 7. EGFP-YAP nuclear condensate localization with RNAPII during sorbitol treatment.

(a-c) Immunofluorescence images and line plot of indicated regions showing EGFP-YAP localization with RNAPII (pSer2) in different conditions. (d-f) EGFP-YAP localization with nascent RNA pulse-labelled by EU for 5min, and visualized by Click-iT chemistry. RNA is shown in the Fire look-up table in ImageJ. Line plots of EGFP-YAP condensate localization with nascent RNA signal are shown below. Scale bars in whole-nucleus view: 5μm. Scale bars in condensate view: 1μm. All the experiments are repeated 3 times independently with similar results. Numerical source data are provided in Source Data Figure 7.

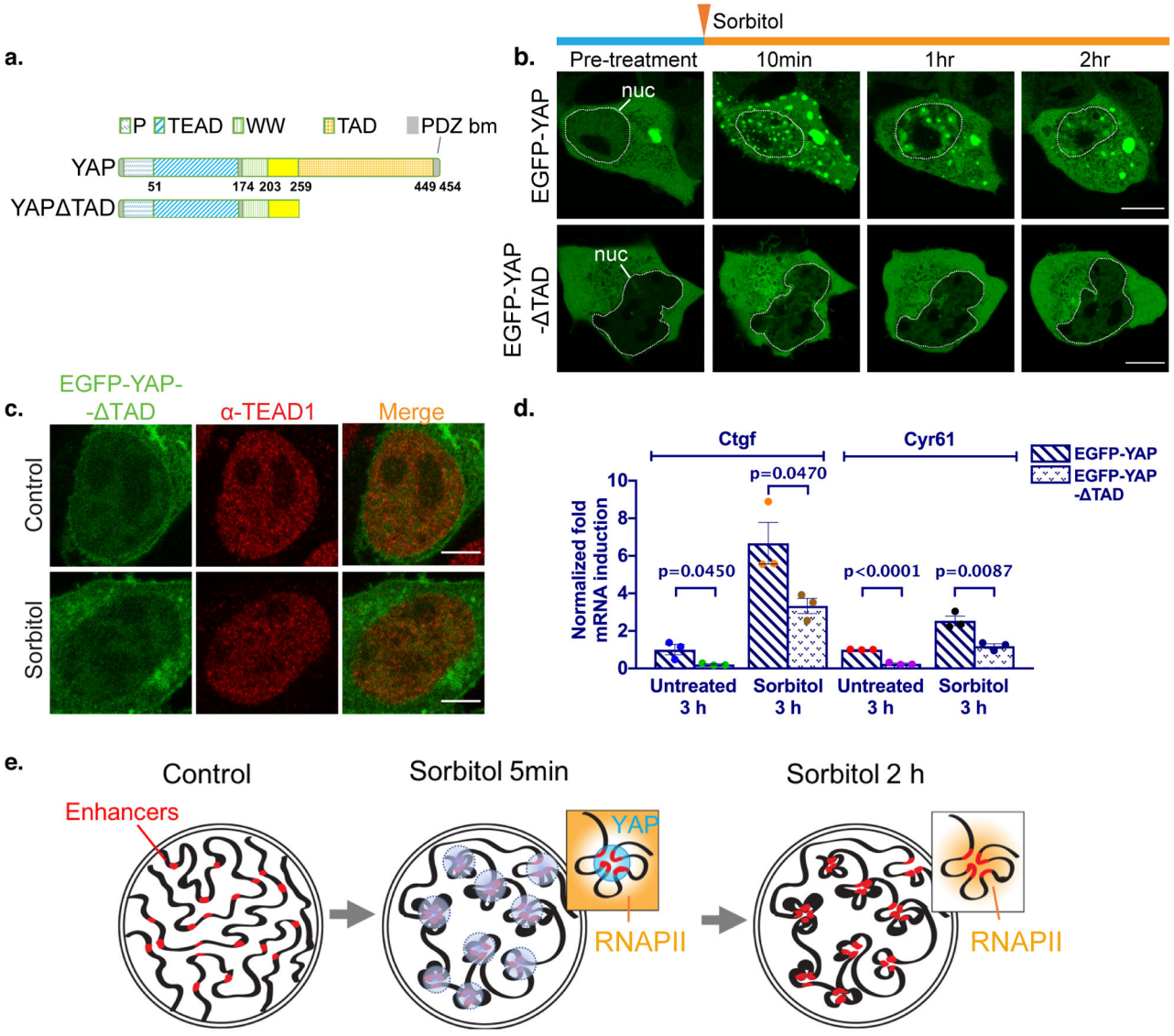

Fig. 8. Phase separation of YAP is important for its nuclear localization and signaling.

(a) Illustration of wildtype YAP (isoform 3, uniprot identifier: P46937-3) and YAPΔTAD structures. Numbers show amino acid position in the wildtype YAP. (b) Live-cell imaging showing time-dependent phase separation of EGFP-YAP variants in HEK293T cells. Scale bars: 10μm. (c) Immunofluorescence image of relative localization of EGFP-YAPΔTAD with TEAD1 in control or 0.2M sorbitol-treated HEK293T cells. Scale bars: 5μm. The experiment is repeated 3 times independently with similar results. (d) Quantification of RT-PCR results showing relative Ctgf and Cyr61 mRNA expressions in HEK293T cells expressing EGFP-YAP variants after indicated treatments. Center of the data is mean. Two-sided unpaired t-test. Error bars show SEM. n= 3 biologically independent experiments. (e) Model depicting remodeling of enhancer elements by YAP phase separation. Statistics source data are provided in Source Data Figure 8.